scientific reports

Check for updates

OPEN

Design and simulation of $CsPb._{625}Zn._{375}IBr_2$-based perovskite solar cells with different charge transport layers for efficiency enhancement

M. Khalid Hossain[1,2]✉, Md Aminul Islam[3], M. Shihab Uddin[4], Prabhu Paramasivam[5,6]✉, Junainah Abd Hamid[7], Razan A. Alshgari[8], V. K. Mishra[9]✉ & Rajesh Haldhar[9]✉

In this work, $CsPb._{625}Zn._{375}IBr_2$-based perovskite solar cells (PSCs) are numerically simulated and optimized under ideal lighting conditions using the SCAPS-1D simulator. We investigate how various hole transport layers (HTL) including Zn_3P_2, PTAA, MoS_2, MoO_3, MEH-PPV, GaAs, $CuAlO_2$, Cu_2Te, ZnTe, $MoTe_2$, CMTS, CNTS, CZTS, CZTSe and electron transport layers (ETL) such as CdS, SnS_2, ZnSe, $PC_{60}BM$ interact with the devices' functionality. Following HTL material optimization, a maximum power conversion efficiency (PCE) of 16.59% was observed for the FTO/SnS_2/$CsPb._{625}Zn._{375}IBr_2$/$MoS_2$/Au structure, with MoS_2 proving to be a more economical option. The remainder of the investigation is done following the HTL optimization. We study how the performance of the PSC is affected by varying the materials of the ETL and to improve the PCE of the device, we finally optimized the thickness, charge carrier densities, and defect densities of the absorber, ETL, and HTL. In the end, the optimized arrangement produced a V_{OC} of 0.583 V, a J_{SC} of 43.95 mA/cm^2, an FF of 82.17%, and a PCE of 21.05% for the FTO/ZnSe/$CsPb._{625}Zn._{375}IBr_2$/$MoS_2$/Au structure. We also examine the effects of temperature, shunt resistance, series resistance, generation rate, recombination rate, current-voltage (JV) curve, and quantum efficiency (QE) properties to learn more about the performance of the optimized device. At 300 K, the optimized device provides the highest thermal stability. Our research shows the promise of $CsPb._{625}Zn._{375}IBr_2$-based PSCs and offers insightful information for further development and improvement.

Keywords Double perovskite solar cell, $CsPb._{625}Zn._{375}IBr_2$ light absorber, ZnSe ETL, MoS_2 HTL, SCAPS-1D

Perovskite solar cells (PSCs) are regarded as one of the more viable variants for harnessing solar energy due to their appealing bandgap, high carrier mobility, and high absorption coefficient, among other desired optoelectronic attributes[1–4]. PSCs present a cost-effective and straightforward deposition method for harvesting solar energy compared to silicon solar cells[5–8]. Moreover, the power conversion efficiency (PCE) of PSCs has risen dramatically throughout the preceding 12 years, rising from 3.8 to 26.1%, enabling them to contend with silicon solar cells[9–11].

The perovskite material has the chemical formula ABX_3, where A represents an organic cation [CH_3NH^{3+}], B represents a divalent metal ion (Pb^{2-}, Sn^{2-}), and X (Br^-, I^-, Cl^-) represents a halide ion when positioned at

[1]Institute of Electronics, Atomic Energy Research Establishment, Bangladesh Atomic Energy Commission, Dhaka 1349, Bangladesh. [2]Department of Advanced Energy Engineering Science, Interdisciplinary Graduate School of Engineering Sciences, Kyushu University, Fukuoka 816-8580, Japan. [3]School of Electrical, Computer and Energy Engineering, Arizona State University, Tempe, AZ 85281, USA. [4]Department of Electrical and Electronic Engineering, Islamic University, Kushtia 7000, Bangladesh. [5]Centre for Research Impact & Outcome, Chitkara University Institute of Engineering and Technology, Chitkara University, Rajpura, Punjab 140401, India. [6]Department of Mechanical Engineering, Mattu University, Mettu 318, Ethiopia. [7]Management and Science University, Shah Alam, Selangor, Malaysia. [8]Chemistry Department, College of Science, King Saud University, Riyadh 11451, Saudi Arabia. [9]School of Chemical Engineering, Yeungnam University, Gyeongsan 38541, Republic of Korea. ✉email: khalid.baec@gmail.com; khalid@kyudai.jp; prabhu.paramasivam@meu.edu.et; mishravlm30@gmail.com; rajeshhaldhar.lpu@gmail.com

the body middle of the octahedron, six halide anions surround cation B, which has favorable bandgaps, high absorption coefficient, lingering carrier diffusion length, exalted carrier mobility, and superb carrier lifetime[12,13]. However, despite exhibiting excellent optoelectronic properties and evolutionary success in PCE within a very short time, the lack of lingering-term stability is still taken into account as the biggest hindrance to making PSCs commercially available[14]. Under the influence of UV light, redox reactions trigger chemical decomposition. Moreover, the polarity of water molecules adversely affects the hydrogen bonds of perovskites[15,16]. As a result, the stability of PSCs decreases when they are exposed to moisture, UV light, and the surrounding environment. This leads to an inevitable deterioration in PSC performance within a few weeks[15–17]. Therefore, improving the stability of perovskite has taken special attention in recent years so that stable PSCs can be achieved without compromising performance.

Different strategies are investigated to address these issues and improve perovskite stability. Two-dimensional (2D) perovskite and inorganic perovskite are possible solutions to the stability issues[18–20]. However, 2D perovskite is not an ideal option for developing high-performance PSCs due to its huge bandgaps, asymmetric crystallographic orientations, as well as lengthy organic cation layers, which limit high carrier generation and slow effective charge carrier separation[12,21]. So, inorganic perovskite materials can be used in solar cells to improve the PSC's steadiness and retain their efficiency[22,23]. Cesium ions (Cs^+) can be used as a replacement for organic cations to enhance the resilience of materials composed of perovskites[20]. In 2012, Cs-based $CsSnI_3$ perovskite was introduced, achieving an efficiency of 0.88%[24]. Since then, many cesium lead halide perovskites have been formed to be utilized in perovskite solar cells (PSCs), including $CsPbI_3$, $CsPbBr_3$, and $CsPbCl_3$[25–29]. $CsPbI_3$ has demonstrated a maximum PCE of ~19% as of 2021[30]. The PCE of $CsPbX_3$-based devices is still lower than that of their organic-inorganic counterparts, even with the notable advancements in this area. So, to take into account the benefits of inorganic perovskites' inherent photostability and ensure the achievement of high efficiency of a single-cell structure and cutting-edge approaches like replacing the materials.

PSCs comprised of a $CsPb._{625}Zn._{375}IBr_2$ absorber layer are promising because of their opt electrical properties[31,32]. Based on our knowledge, $CsPb_{0.625}Zn_{0.375}IBr_2$ absorber material has not yet been explored experimentally. However, similar halide perovskites, such as $CsSn_xGe_{1-x}IyBr_{3-y}$, $CsPb_xSn_{1-x}IyBr_{3-y}$ have been successfully synthesized and studied in experimental setups[33–35]. Prior studies have identified several significant challenges during fabrication, including maintaining stability, preventing defects, achieving homogeneous morphology, and controlling stoichiometry[36]. According to those investigations, maximizing the characteristics and device performance of these above-mentioned perovskites requires controlling morphological defects, such as surfaces or heterointerfaces, intragrain defects, and grain boundaries[37,38]. Achieving a high-quality perovskite thin film with characteristics such as dense, uniform, pinhole-free layers, large grain sizes, and low grain boundary density has proven beneficial for device performance. Common fabrication methods such as one-step spin-coating and two-step deposition also have been employed to synthesize these perovskite thin films for achieving high-quality uniform layers. To enhance stability especially additive engineering has been applied in similar perovskite films, which may also be applicable to $CsPb_{0.625}Zn_{0.375}IBr_2$[39,40].

In addition, the determination of adequate ETL and HTL amalgamation can significantly contribute towards increasing the PCE of these emerging devices[41–43]. Moreover, the thicknesses of the ETL HTL, along with their interface and phase-matching properties, profoundly impact solar metrics including PCE, fill factor (FF), short-circuit current density (J_{SC}), and open-circuit voltage (V_{OC})[41–45].

Specifically, the ETL is an indispensable aspect of a PSC because it extracts electrons from the perovskite absorber and inhibits holes in it. To further boost the PCE of PSC, the scientific community has been meticulously tracking the introduction of new materials through the previously indicated pathway, especially in ETL. TiO_2, ZnO, and SnO_2 are examined extensively for PSCs[46–49]. New ETLs are still one of the major concerns in the research community. Recently, Liu et al. achieved 11.2% efficiency with all-low-temperature processed PSCs using CdS as ETL. Peng et al. reported an even higher efficiency of 15%[50]. Tin Sulfide (SnS_2) is a cost-effective metal sulfide with unique chemical and structural properties, making tunable bandgap ideal for PSC[51]. After studying Mg-doped ZnO (MZO) and the impact of Mg concentration on their optical characteristics and structure, it was determined that Mg-doped ZnO films could be appropriate for PSCs[52]. Zinc Selenide (ZnSe) has been devoted as an ETL in PSCs due to its excellent electron mobility and 2.8 eV straight bandgap. It might function as an n-type collecting layer for reliable and productive commercial PSCs[53]. PSCs with as-deposited [6, 6]-phenyl-C60-butyric acid methyl ester ($PC_{60}BM$) layer displayed no photocurrent hysteresis, even without thermal treatment[54]. So, in comparative analysis, these five ETLs performed superbly in PSCs.

Conversely, though, the HTL impacts solar device manufacturing costs, stability, and efficacy. Materials that are both organic and inorganic are utilized to find the more efficient, stable, and low-cost HTLs[55–57]. However, recent research shows that the superior band alignment, affordability, and stability of inorganic and small molecule HTLs contribute to improved solar cell performance[58–63]. Different organic and inorganic HTLs, Zinc Phosphide (Zn_3P_2), Poly[bis(4-phenyl)(2,4,6-trimethylphenyl)amine (PTAA), Molybdenum disulfide (MoS_2), Molybdenum trioxide (MoO_3), Poly[2-methoxy-5-(2'-ethylhexyloxy)-1,4-phenylene vinylene] (MEH-PPV), Gallium arsenide (GaAs), Copper aluminum oxide ($CuAlO_2$), Copper Telluride (Cu_2Te), Zinc Telluride (ZnTe), Molybdenum Telluride ($MoTe_2$), Copper zinc tin sulfide (CZTS), copper zinc tin selenide (CZTSe), copper manganese tin sulfide (CMTS), and copper-nickel tin sulfide (CNTS) will be analyzed in PSCs because of its tunable band gap.

In this work, we outline the layout and execution of a $CsPb._{625}Zn._{375}IBr_2$ -based perovskite-based solar cell using a unique device architecture: FTO/ETL/$CsPb._{625}Zn._{375}IBr_2$/HTL/Au. This work considers HTLs Zn_3P_2, PTAA, MoS_2, MoO_3, MEH-PPV, GaAs, $CuAlO_2$, Cu_2Te, ZnTe, $MoTe_2$, CMTS, CNTS, CZTS, CZTSe as HTLs, CdS, SnS_2, ZnSe, $PC_{60}BM$ as ETLs. To leverage optimal cell output, we offer detailed investigations of the effects of the degree of doping and ETL/HTL layer thickness, perovskite interface layers, electron/hole transport layer separation, absorber layer thickness, and perovskite defect density on PV parameters using the SCAPS-1D in this

work[64]. Furthermore, the ramifications of recombination rates, J-V, QE, operating temperature, and series and shunt resistance were assessed in PV performance generation. Finally, a comparison with earlier research was done using the discovered solar cell characteristics. These results imply that our method of device optimization offers a special set of abilities to PSC research that may be used in a real-world device fabrication process in the lab, saving the researchers money and time.

Device modeling and device structure

Device modeling

SCAPS-1D has been employed to simulate the device characteristics of perovskite-based solar cells. With SCAPS-1D, a strong correlation between simulation and experimental data could be demonstrated[65]. The SCAPS-1D software for simulating optoelectronic devices was developed by the Department of Electronics and Information Systems (ELIS) at the University of Gent[64]. SCAPS is frequently employed in simulations of optoelectronic devices, notably for solar energy device research since it is capable of resolving the Poisson equations. (Eq. 1) and continuity equations (Eqs. 2–3) to estimate PV device output[64].

$$\frac{\partial}{\partial x}\left(\epsilon \frac{\partial \psi}{\partial x}\right) = -q\left[p - n + N_D^+ - N_A^- + \frac{\rho_{def}}{q}\right] \tag{1}$$

$$\frac{\partial n}{\partial x} = -\frac{\partial J_n}{\partial x} + G - R_n \tag{2}$$

$$\frac{\partial p}{\partial x} = -\frac{\partial J_p}{\partial x} + G - R_p \tag{3}$$

Where J_n and J_p are considered electron and hole concentrations respectively. Which are described in (Eqs. 4–5).

$$J_n = -\frac{\mu_n n}{q}\frac{\partial E_{Fn}}{\partial x} \tag{4}$$

$$J_p = +\frac{\mu_p p}{q}\frac{\partial E_{Fp}}{\partial x} \tag{5}$$

SCAPS may accept seven distinct material layers and front and back contact layers. Furthermore, SCAPS contextualizes and provides an impeccable venue for this research due to its user-friendly options, which include various defect energy distributions (Gauss, Uniform, tail, single level, or combination), intricate defect shapes (interface or bulk defect), and defect charge types (idealization, monovalent, divalent, and multivalent)[64]. Photovoltaic characteristics (efficiency, J_{SC}, FF, and V_{OC}) with defect density (Eqs. 6–10) to forecast PSCs characteristics[2].

$$L = \sqrt{D\tau} \tag{6}$$

$$D = \frac{\mu K_B T}{q} \tag{7}$$

$$\tau = \frac{1}{N_T \delta \vartheta_{th}} \tag{8}$$

$$FF = \frac{v_{oc} - \ln(v_{oc} + 0.72)}{v_{oc}} \tag{9}$$

$$V_{oc} = \frac{nKT}{q} v_{oc} \tag{10}$$

This study focuses on device optimization based on the PV parameters of solar cell devices. SCAPS-1D is a powerful simulator that can model the electrical characteristics of solar cells[66–69], including current-voltage (I-V) curves, capacitance-voltage (C-V) relationships, capacitance-frequency (C-f) responses, quantum efficiency profiles, and so on. Such electrical modeling plays a crucial role in determining solar cell device performance, enabling the optimization of parameters like layer thickness, doping density, and defect density. However, it is important to acknowledge that optical simulations also play a critical role in optimizing the design of solar cells as supported by previous studies[70,71]. Optical modeling not only enables more accurate calculations of layer thicknesses but also provides valuable insights into material selection for enhancing light absorption and minimizing reflection. Three macroscopic parameters including photon absorption, the energy band gap of the material, and device resistance—are crucial for determining power-conversion efficiency[72–75]. Additionally, in thin-film solar cells, optical interference effects significantly influence light absorption, underscoring the necessity of optical modeling for improving absorption efficiency. However, optical modeling was omitted in this study as our primary objective was to establish a solid understanding of the device's electrical characteristics.

Device structure

An n-i-p planar heterojunction structure consisting of the ETL, HTL $CsPb._{625}Zn._{375}IBr_2$ absorber, transparent Fluorine doped tin oxide (FTO), and gold (Au) back contact was simulated on SCAPS-1D for this investigation, as shown in Fig. 1. In every device structure, the absorber layer $CsPb._{625}Zn._{375}IBr_2$ lies in the space between the

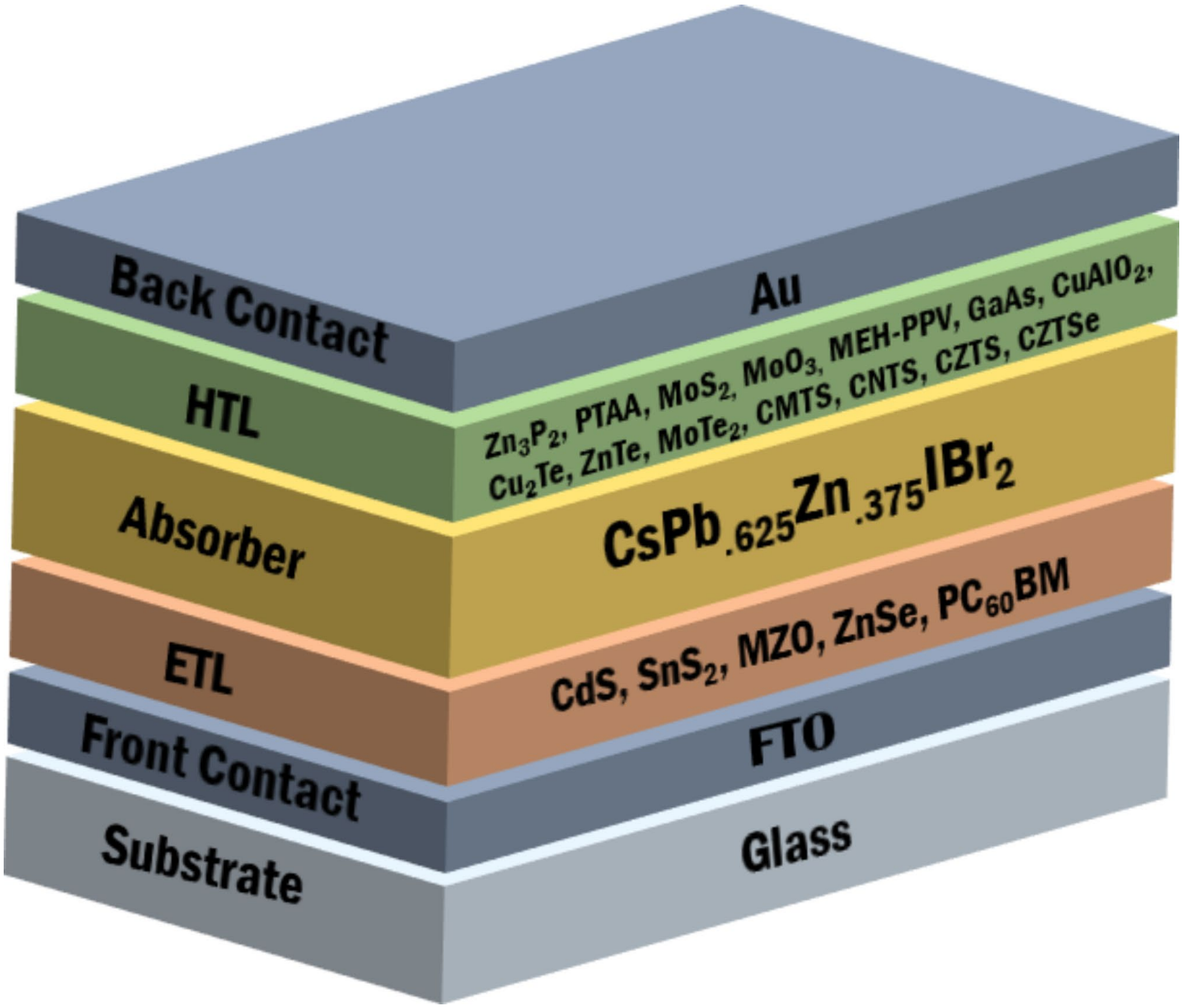

Fig. 1. PSC structure based on $CsPb_{.625}Zn_{.375}IBr_2$ absorber.

HTL and the ETL. The p-region is represented by the HTL, the i-region by the $CsPb_{.625}Zn_{.375}IBr_2$ absorber, and the n-region by the ETL. When exposed to light, the absorber layer of the solar cell forms electron-hole pairs, with the electrons and holes moving in the directions of the n- and p-layers, respectively. Electrons and holes can migrate and separate because of the electrical field that exists beneath the two layers.

The study examines the efficacy and efficiency of ten HTL and four ETL-based optimized PSC structures. As used in the SCAPS-1D simulation in this work, Tables 1 and 2 displays the optoelectronic properties of the FTO, ETLs (CdS, SnS_2, ZnSe, $PC_{60}BM$), absorber layer ($CsPb_{.625}Zn_{.375}IBr_2$), and HTLs ($Zn_3P_2$, PTAA, MoS_2, MoO_3, MEH-PPV, GaAs, $CuAlO_2$, Cu_2Te, ZnTe, $MoTe_2$, CMTS, CNTS, CZTS, CZTSe). With 4.4 eV of work function, an FTO is utilized and the thickness of FTO is assumed to be 200 nm. Device performance is optimized by varying the thickness of the absorber, HTL, and ETL layers across a wide range. The temperature at which the simulation runs is 300 K under a single sun's radiation (100 mW/cm^2, AM1.5G).

Result and discussion

Impact of different HTL materials on PSC performance

HTL is one of the important factors for achieving high-performance PSCs. Their main purpose is to minimize charge recombination by effectively extracting and transporting photo-generated holes from the perovskite material to the back electrode. For a material to be considered an effective hole transport material, it must fulfill several important requirements. The HTL and the perovskite material should have a favorable energy level alignment for effective hole extraction. It should also have outstanding conductivity and high hole mobility to facilitate efficient charge transfer[87]. Inorganic and organic materials are used to find the best HTL for $CsPb_{.625}Zn_{.375}IBr_2$-based PSC. In the beginning, we selected SnS_2 as ETL and designed the device FTO/SnS_2/$CsPb_{.625}Zn_{.375}IBr_2$/HTL/Au. We varied HTLs (Zn_3P_2, PTAA, MoS_2, MoO_3, MEH-PPV, GaAs, $CuAlO_2$, Cu_2Te, ZnTe, CNTS) to get the best HTL material for our device. In PSCs, characteristics of HTL like bandgap, band

Material property	FTO	SnS_2	ZnSe	CdS	$PC_{60}BM$	$CsPb_{0.625}Zn_{0.375}IBr_2$ (absorber)
Thickness (nm)	200	150	70	50	50	50–500 nm
Bandgap, *Eg* (eV)	3.5	1.85	2.81	2.4	1.8	1.05
Electron affinity, X (eV)	4.00	4.26	4.09	4.18	4.2	4.27
Relative dielectric permittivity, εr	9.00	17.7	8.6	10	4	6
Conduction band effective density of states N_C (1/cm^3)	2.2×10^{18}	7.32×10^{18}	2.2×10^{18}	2.2×10^{18}	1×10^{21}	1×10^{19}
Valence band effective density of states N_V (1/cm^3)	1.8×10^{19}	1×10^{19}	1.8×10^{18}	$1\,0.9\times 10^{19}$	2×10^{20}	1×10^{19}
Electron thermal velocity (cm s^{-1})	10^7	10^7	10^7	10^7	10^7	10^7
Hole thermal velocity (cm s^{-1})	10^7	10^7	10^7	10^7	10^7	10^7
Electron mobility, μn (cm^2/Vs)	20	50	4×10^2	100	0.1	25
Hole mobility, μh (cm^2/Vs)	10	25	1.1×10^2	25	0.1	25
Donor density, N_D (1/cm3)	10^{18}	9.85×10^{19}	1×10^{18}	1×10^{18}	1×10^{17}	1×10^{15}
Acceptor density, N_A (1/cm^3)	0	0	0	0	0	1×10^{15}
Total density (cm^{-3})	10^{15}	10^{14}	1×10^{15}	1×10^{15}	1×10^{15}	1×10^{12}
Reference	76	77	76	78	79	32

Table 1. Input parameters of the FTO, absorber, and ETL in this study.

Material property	PTAA	GaAs	ZnTe	CNTS	MoO_3	MEH-PPV	$CuAlO_2$	MoS_2	Cu_2Te	Zn_3P_2
Thickness (nm)	150	150	250	100	100	50	350	200	250	250
Bandgap, *Eg* (eV)	2.96	1.42	2.25	1.74	3.0	2.1	3.46	1.29	1.18	1.5
Electron affinity, X (eV)	2.3	4.07	3.73	3.87	2.3	2.8	2.5	4.2	4.2	4.2
Relative dielectric permittivity, εr	9	12.9	7.3	9	18	3	60	3	10	7.11
Conduction band effective density of states N_C (1/cm^3)	2.0×10^{21}	2.2×10^{18}	2.2×10^{18}	2.2×10^{18}	1×10^{19}	2.5×10^{19}	2.2×10^{18}	2.2×10^{18}	7.8×10^{17}	2.2×10^{18}
Valence band effective density of states N_V (1/cm^3)	2.0×10^{21}	1.8×10^{19}	1.8×10^{19}	1.8×10^{19}	2.2×10^{18}	2.5×10^{19}	1.8×10^{19}	1.9×10^{19}	1.6×10^{19}	1.8×10^{19}
Electron thermal velocity (cm s^{-1})	10^7	10^7	10^7	10^7	10^7	10^7	10^7	10^7	10^7	10^7
Hole thermal velocity (cm s^{-1})	10^7	10^7	10^7	10^7	10^7	10^7	10^7	10^7	10^7	10^7
Electron mobility, μn (cm^2/Vs)	1	8500	300	11	210	0.5×10^{-4}	2	100	500	1
Hole mobility, μh (cm^2/Vs)	40	400	100	11	210	0.5×10^{-5}	8.6	150	100	10
Donor density, N_D (1/cm3)	0	0			0	0	0	0	0	0
Acceptor density, N_A (1/cm^3)	1×10^{18}	1×10^{11}	1.0×10^{16}	1.0×10^{19}	1×10^{18}	1×10^{15}	3×10^{18}	1×10^{17}	1.0×10^{21}	1.0×10^{19}
Total density (cm^{-3})	Acceptor 1×10^{15}	1×10^{14}	1×10^{14}	1×10^{14}	1×10^{15}	1×10^{15}	1×10^{15}	1×10^{14}	1×10^{14}	1.0×10^{14}
Reference	77	80	81	82	83	84	76	85	81	86

Table 2. Input parameters of HTL in this study.

offset, and carrier mobility are considered prevalent roles for getting high efficiency. Valence band offset. Among all of them, valence band offset (VBO) is particularly important and can be measured from the contrast between the absorber's valence band and HTL and described in Eqs. 11–12 [88].

$$\chi_{absorber} + E_{g_{absorber}} \geq \chi_{HTL} + E_{g_{HTL}} \; ; \; Negative\, VBO \tag{11}$$

$$\chi_{absorber} + E_{g_{absorber}} \leq \chi_{HTL} + E_{g_{HTL}} \; ; \; Positive\, VBO \tag{12}$$

When VBO becomes negative, a cliff forms between the interface of the absorber and HTL. This cliff does not create a problem with to flow hole toward the electrode. Nevertheless, carrier recombination's activation energy diminishes and increases the recombination rate[88]. When VBO becomes positive a spike appears at the HTL and absorber interfaces, blocking hole flow to the electrode but, the carrier recombination will probably be reduced. The performance of the cell is negatively impacted if VBO increases because it creates an energy barrier that prevents photogenerated holes from accessing the electrode[88]. However, highly negative VBO raises the energy

barrier at the interface, which results in inefficient charge transfer and decreases the device's performance. Due to the increased barrier, surface recombination is encouraged, which lowers the open-circuit voltage and overall device efficiency[89,90].

Following the evaluation of various HTL materials on PSCs performance, the device incorporating MoS_2 HTL exhibited the highest PCE, as shown in Fig. 2. This superior performance prompted the selection of MoS_2 as the HTL for further numerical analysis. A positive VBO (+0.15 eV) creates a spike that reduces the carrier recombination and gets a higher efficiency (16.59%) compared to the other HTL.

Band diagram and ETL dependent device performance

The band alignment of the $CsPb._{625}Zn._{375}IBr_2$-based PSC device setup is shown in Fig. 3, where the MoS_2 HTL and SnS_2, $PC_{60}BM$, ZnSe, and CdS are utilized as the ETLs. The absorbing layer of each ETL and HTL is used by the valence band offset to be impacted by the energy band diagram and conduction band offset, respectively. The energy level alignment impacts the performance of PSCs. In the PSCs, the flow of electrons is introduced into the matching ETL conduction band while holes are concurrently transported to the HTL[91]. Subsequently, the corresponding Au and FTO are where holes and electrons are gathered, respectively.

The efficiency of PSCs is profoundly impacted by the energy-level alignment. Photogenerated electrons are simultaneously transported to the HTL by holes and injected into the ETL conduction band in PSCs. Subsequently, the front (FTO) and rear (Au) contact metals accumulate electrons and holes, respectively. The ionization energy of HTL must be less than $CsPb._{625}Zn._{375}IBr_2$, and ETL's electron affinity must be greater than the $CsPb._{625}Zn._{375}IBr_2$, to extract the holes at the $CsPb._{625}Zn._{375}IBr_2$/HTL interface. Key performance measures of the device, including the J_{SC}, V_{OC}, FF, and PCE, are also profoundly altered by the mismatch in energy bands at the ETL/$CsPb._{625}Zn._{375}IBr_2$ and $CsPb._{625}Zn._{375}IBr_2$/HTL interface[91]. The Fermi levels adjacent to the band of valence differ from one another, as Fig. 3 illustrates, but they are in proximity to the conduction band and progressively penetrate it in all four scenarios. Figure 3 displays the energy band map for four distinct solar cell architectures: SnS_2, CdS, ZnSe, and $PC_{60}BM$ as ETL. The HTL (MoS_2) and the built-in potential of the absorber interface are important factors in influencing the J_{SC} and V_{OC} of PSCs. Electron transport, or the movement

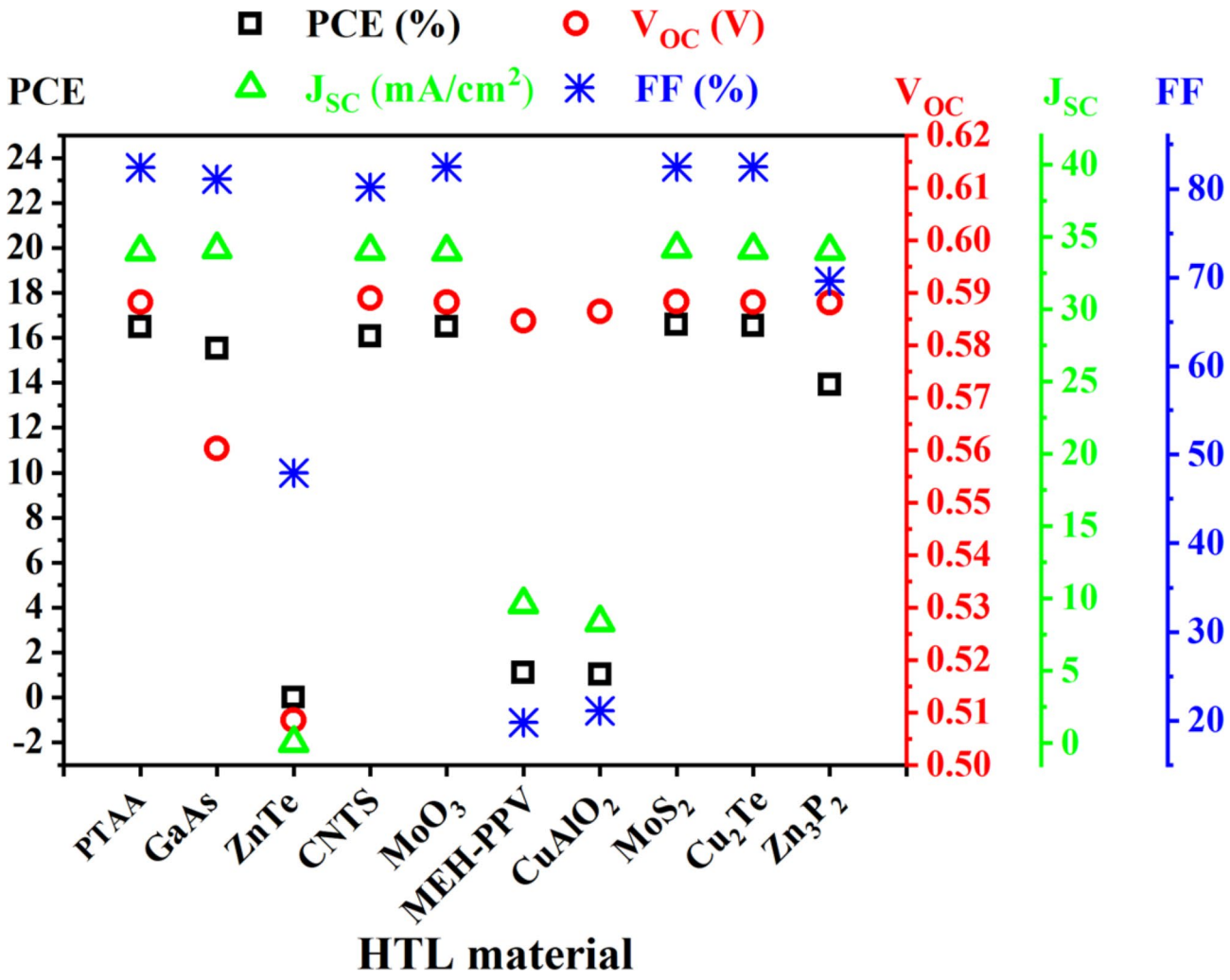

Fig. 2. Impact of different HTL materials on device performance.

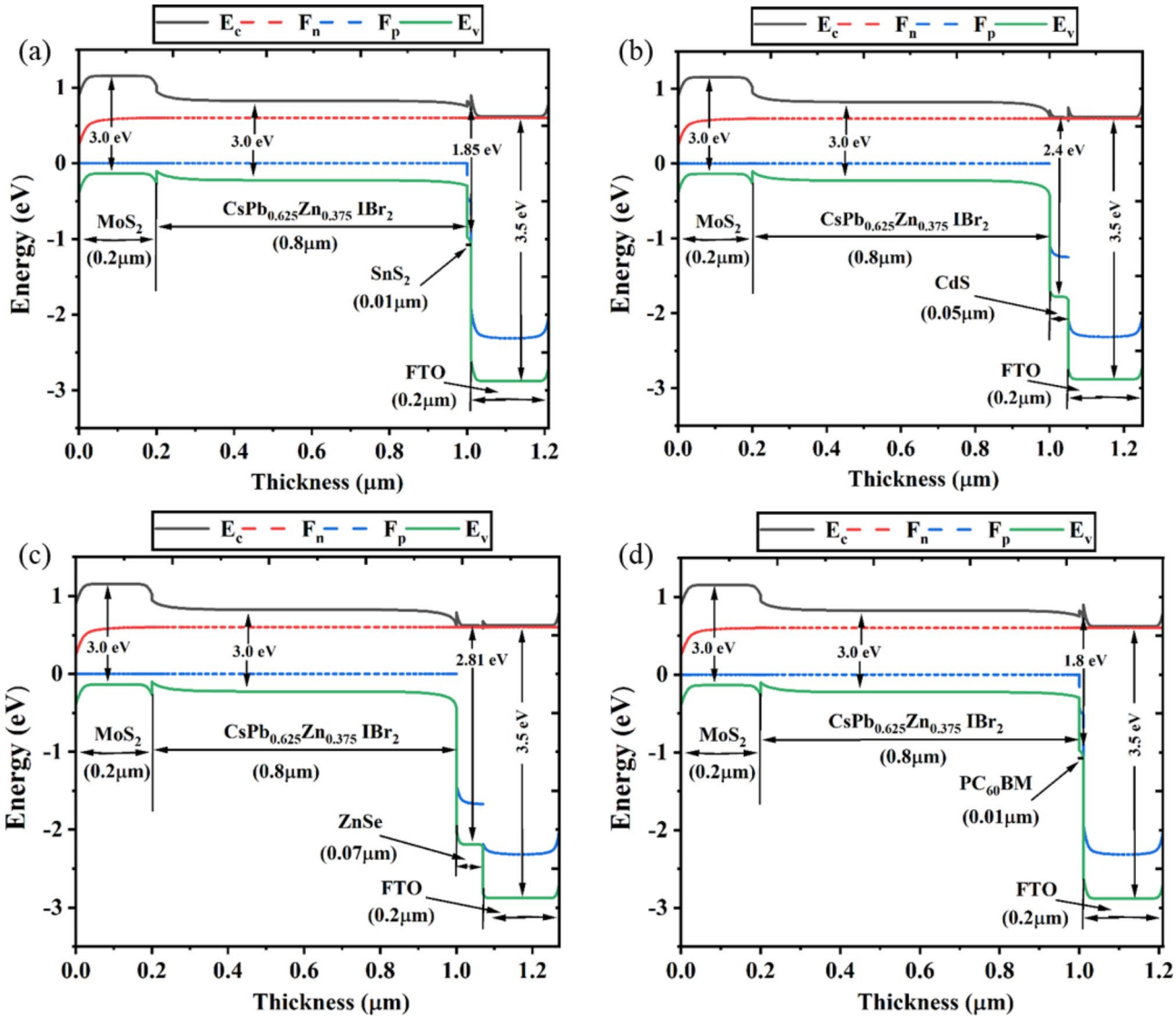

Fig. 3. Energy band diagram of PSCs with distinct ETLs as (**a**) SnS_2, (**b**) CdS, (**c**) ZnSe, (**d**) $PC_{60}BM$.

of negative charge carriers from the perovskite layer to the electrode, is the function of the ETL. The J_{SC} and V_{OC} as well as the overall performance of the solar cell can be greatly impacted by the kind and quality of the ETL[91]. An efficient ETL can boost the current density by reducing hole and electron recombination at the contact between the ETL and the perovskite layer[91]. However, to understand the band alignment between the absorber and different ETLs, it is crucial to analyze the Conduction Band Offset (CBO), which can be calculated as $\mathrm{CBO} = \chi_{\mathrm{abs}} - \chi_{\mathrm{ETL}}$[92]. A positive CBO results in a spike-like band alignment, where the absorber's conduction band is lower than that of the ETL. In contrast, a negative CBO leads to a cliff-like band alignment, where the absorber's conduction band is higher than the ETL's. As shown in Fig. 3, most ETL devices exhibit a negative CBO, indicating smoother electron extraction from the absorber to ETL[93,94]. Due to variations of work function in the ETL and absorber, an almost entirely depleted absorber layer forms in the $CsPb_{.625}Zn_{.375}IBr_2$-based device, as seen in Fig. 3. The passage of charge carriers within the PSCs was influenced by the internal electric field created by this depleted absorber layer. Higher short circuit current (J_{SC}) is the outcome of a fully depleted absorber layer; however, a lower V_{OC} value is caused by an inadequate offset between the absorber/HTL and the quasi-fermi level from the ETL/absorber[91].

Optimization of absorber, ETL, and HTL thickness

Impact of absorber thickness

The absorber layer's thickness has a major impact on how well PSC functions. Figure 4 FTO/ETL/$CsPb_{.625}Zn_{.375}IBr_2$/$MoS_2$/Au PSCs are analyzed with varying absorber, ETL, and HTL thicknesses. Figure 4a illustrates the impact of absorber thickness by varying the absorber's thickness ranges from 0.5 μm to 1.5 μm. V_{OC} changes ridiculously small when the thickness is varied. When the thickness is 0.5 μm V_{OC} is almost 0.593 V and after increasing the thickness V_{OC} decreases and reaches 0.562 V. This agrees well with values that have been

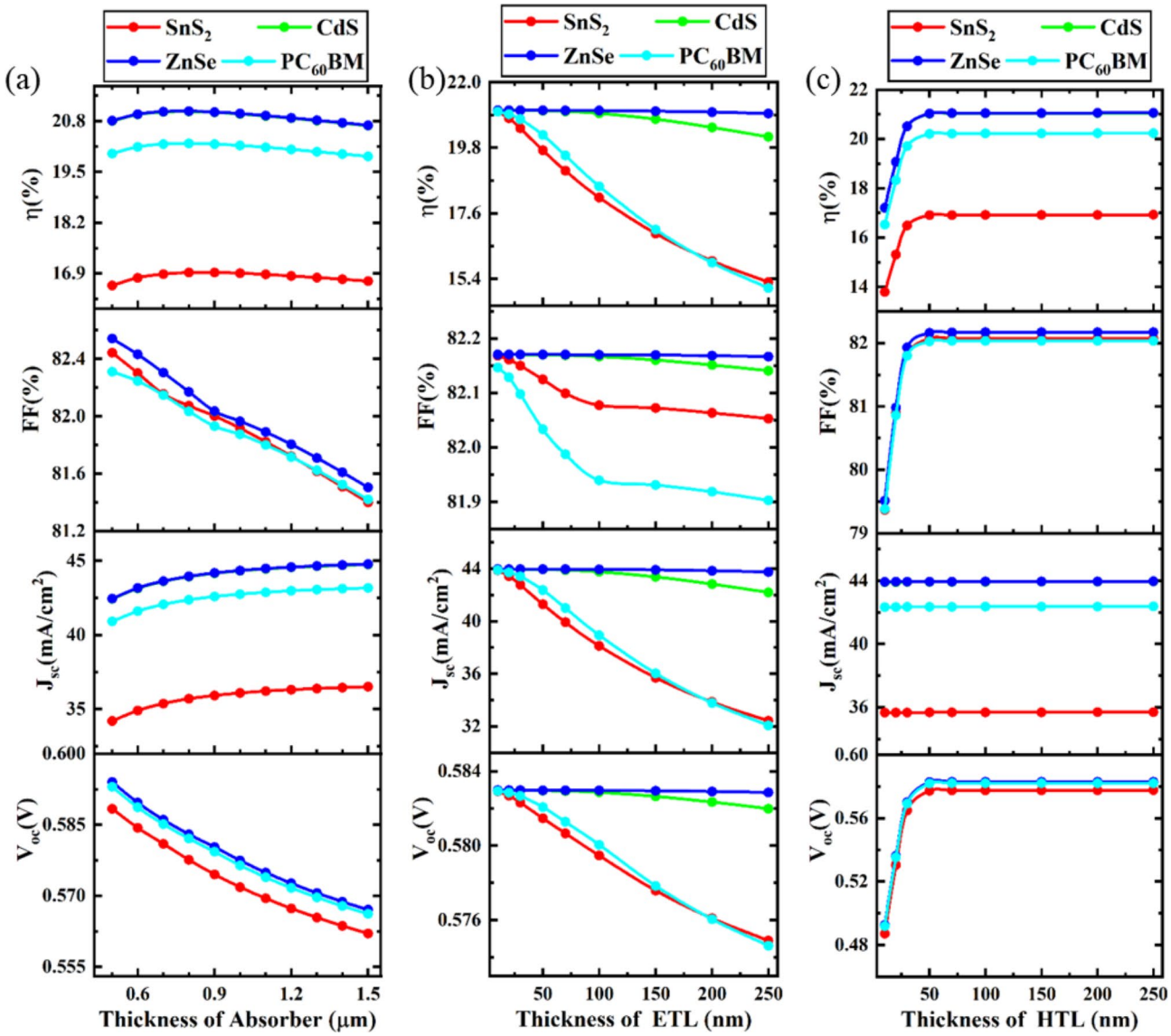

Fig. 4. Impact of the absorber, ETL, and HTL thickness on device performance.

previously published[7,95]. According to Fig. 4a, J_{SC} rises as absorber thickness increases. The photogeneration of excitons and light absorption are responsible for this increase in J_{SC}. Due to its comparatively poor absorption, a thin absorber layer produces few electron-hole pairs at a large wavelength range. As the perovskite absorber's thickness expands, the long wavelength absorption rises, improving exciton pair formation. In all four different ETL configurations, J_{SC} is increasing with thickness increments[7,95]. However, in solar cell configurations, increasing thickness adds to the series resistance, resulting in substantial carrier recombination losses and decreasing FF[96]. Figure 4 shows that PCE and J_{SC} improve up to 700 nm as the absorber layer thickness grows from 0.2 μm to 1 μm, indicating higher creation of electron-hole pairs[97,98]. However, an absorber thickness of 0.8 μm has been maintained for further numerical analysis of all ETL devices where the highest PCE, 21.05%, was achieved for the ZnSe ETL device, with a V_{OC}, J_{SC}, and FF of 0.58 V, 43.94 mA/cm^2, and 82.17%, respectively.

Impact of ETL thickness

Extracting electrons from the absorber surface without allowing holes to recombine is the fundamental and main purpose of the ETL. The varying thicknesses of the ETL will alter the visible light transmittance of the film, as demonstrated in experimental settings. Consequently, the thickness of the ETL is especially important for optimizing the solar cell. The fluctuations in ETL thickness from 0.01 μm to 0.25 μm with the output of PSCs may be improved to illustrate the impact of ETL thickness. It is evident from the results shown in Fig. 4b that the PCE reduces as the ETL becomes thicker for SnS_2, $PC_{60}BM$. This reduction may cause more significant pinholes to form, which reduces the J_{SC}. Moreover, a thicker ETL promotes greater electron-hole recombination, increasing resistance and contributing to a decline in PCE[99]. However, PCE is almost constant for ZnSe and CdS ETL devices and this agrees well with values that have been previously published[100]. In this study, an ETL

thickness of 0.01 μm has been selected as the optimized value for SnS_2 and $PC_{60}BM$-based ETL devices, while thicknesses of 0.05 μm and 0.07 μm are optimized for CdS and ZnSe ETL devices, respectively. These values were maintained in further numerical analyses. Among the four ETL configurations, the ZnSe ETL device achieved the highest PCE of 21.05%, with a V_{OC}, J_{SC}, and FF of 0.58 V, 43.94 mA/cm^2, and 82.17%, respectively.

Impact of HTL thickness

Figure 4c illustrates how performance characteristics in $CsPb._{625}Zn._{375}IBr_2$-based PSCs utilizing ZnSe, $PC_{60}BM$, ZnSe, and CdS as ETLs are affected by varying the thickness of the MoS_2 HTL. To reduce direct contact between the anode and perovskite and enhance performance, it is imperative to modify the HTL thickness. We exclusively look at MoS_2 as the HTL in thickness optimizations. This result suggests that while the device's charge transport properties improved, there may have been an increase in charge recombination, leading to a relatively stable trend in J_{SC}. As the HTL thickness increases, carrier collection improves, resulting in a rise in Voc. Consequently, an upward trend in PCE is observed. As the HTL increased in thickness of MoS_2, Fig. 4c demonstrates that V_{OC}, J_{SC}, FF, and PCE levels remained unchanged for any of the ETLs. Around 21% PCE for ZnSe for 50 nm thickness of MoS_2, and this value is consistent with further increments in the thickness of HTL. Similar findings have been reported in previous studies, where an increase in HTL thickness corresponded with enhanced PCE[2,7,101–103]. However, an HTL thickness of 0.02 μm has been maintained for further numerical analysis across all ETL devices. Notably, the ZnSe ETL device again shows the highest PCE of 21.05%, with a V_{OC} of 0.58 V, J_{SC} of 43.94 mA/cm^2, and FF of 82.17%.

Optimization of the acceptor, donor, and defect density of the absorber

Impact of acceptor density of absorber

Figure 5a provides descriptive observations on the characteristics of performance following acceptor density (N_A) change. N_A varies in $CsPb._{625}Zn._{375}IBr_2$ absorber from 1×10^{13} cm^{-3} to 1×10^{20} cm^{-3}. Four different ETLs (ZnSe, $PC_{60}BM$, ZnSe, and CdS) are analyzed here with MoS_2 HTL. V_{OC}, J_{SC}, FF, and PCE are merely constant for N_A 1×10^{13} cm^{-3} to 1×10^{16} cm^{-3}. So, N_A has no influence on cell performance when the value of N_A is less than 1×10^{16} cm^{-3}. However, when the value of N_A crosses the value of 1×10^{16} cm^{-3}, V_{OC} starts to increase but J_{SC} and FF start to decrease, and overall device efficiency starts to decrease. Higher doping concentrations may degrade the solar cell's active layer by introducing unfavorable shunt pathways through the absorber layer, leading to a reduction in the solar cell's efficiency[104]. The same phenomena are observed in previous works[95,105]. The influence of different types of ETL is limited here. The same characteristics are observed for all types of ETL. However, the optimal absorber acceptor density has been set at 10^5 cm^{-3} across all ETL devices, with the ZnSe ETL device demonstrating comparatively higher performance, achieving a PCE of 21.06%, FF of 82.17%, J_{SC} of 43.94 mA/cm^2, and V_{OC} of 0.58 V.

Impact of donor density of absorber

Figure 5b illustrates the device performance if the donor density (N_D) of absorber $CsPb._{625}Zn._{375}IBr_2$ varies from 1×10^{13} cm^{-3} to 1×10^{20} cm^{-3}. To observe the best device configuration for the absorber $CsPb._{625}Zn._{375}IBr_2$, MoS_2 materials are used for HTL, and four different materials (ZnSe, $PC_{60}BM$, ZnSe, and CdS) are used to get the best performance. Like N_A, the same performance characteristics are absorbed for N_D. As the donor density increases, the electric field at the interfaces strengthens, enhancing the charge separation process. However, performance may decline if this stronger field also leads to increased recombination. Additionally, excessive doping can introduce donor defects and increase non-radiative recombination, which may raise the series resistance in PSCs and consequently reduce the PCE. According to Fig. 5b, when the value of N_D is higher than 1×10^{16} cm^{-3} the PCE starts to diminish. However, for further numerical analysis, the donor density has been set to 10^5 cm^{-3}. The ZnSe ETL device demonstrates superior performance among four investigated devices, with a PCE, FF, J_{SC}, and V_{OC} of 21.06%, 82.17%, 43.94 mA/cm^2, and 0.58 V respectively.

Impact of defect density of absorber

The absorber defect density (N_t) has a substantial influence on PSC efficacy. Higher N_t levels in the absorber layer cause film degradation and pinhole development, leading to increased recombination and decreased stability and PCE. To determine the optimal defect density, the simulation varied the absorber defect density from 1×10^{13} cm^{-3} to 1×10^{18} cm^{-3}.

The plot of photovoltaic parameters (V_{OC}, J_{SC}, FF, PCE) against perovskite defect density is shown in Fig. 5c. The findings demonstrate that when the $CsPb._{625}Zn._{375}IBr_2$ defect density increases, the PCE of the examined PSC device falls. As the fault density increases, V_{OC} reduces linearly, as seen in Fig. 5c. The short diffusion length of the perovskite materials is the cause of this decrease in V_{OC}. The charge carriers are typically trapped by high defect sites in perovskite materials, which shortens their lifespan. Consequently, as this carrier lifetime diminishes, the diffusion length does as well[106]. Nonetheless, J_{SC} exhibits a constant response up to a defect density of around 1×10^{16} cm^{-3}, after which it begins to decline as the absorber layer's defect density increases. This is thus because the J_{SC} is reliant on the pace at which electron-hole pairs are generated. Carrier diffusion is also a factor in J_{SC}, and it gets less with increasing defect density. As a result, J_{SC} falls as fault density increases. However, because of the short diffusion length, it dramatically decreases if the defect density surpasses 1×10^{16} cm^{-3}[107]. From this observation, it is observed that up to 1×10^{14} cm^{-3} absorber defect density is tolerable beyond this value the performance starts to decrease. The same trends are observed in previously reported articles[105,106]. Based on the PV parameters, a defect density of 10^{12} cm^{-3} has been selected as the optimal value for further numerical analysis. Under these conditions, the ZnSe ETL device outperforms the other devices, achieving a PCE of 21.05%, FF of 82.17%, J_{SC} of 43.94 mA/cm^2, and V_{OC} of 0.58 V.

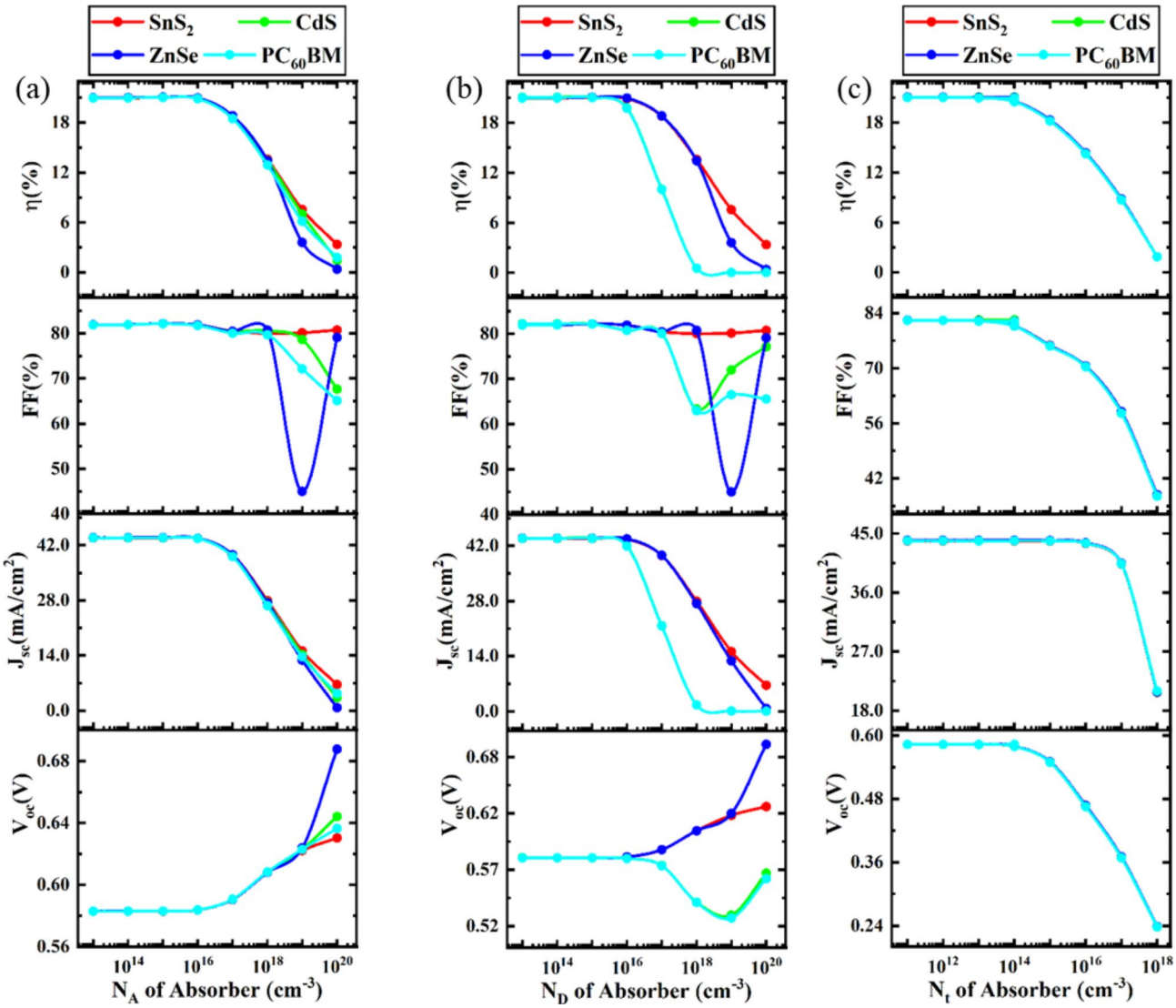

Fig. 5. Impact of acceptor, acceptor, and donor density of absorber on PSC performance.

Optimization of donor and defect density of ETL

Impact of donor density of ETL

The concentration of doping has a major role in separating the charge carriers produced by photolysis. ETL stops hole migration while transferring electrons to the cathode. The electric field that exists at the ETL/absorber contacts and is dependent on the doping density is what separates these charge carriers[108]. This electric field at the interfaces can be strengthened by the doping density concentration in ETL layers. Consequently, when the donor density of ETL grows, the minority carrier concentration is considerably reduced at the interfaces due to a reduction in carrier recombination, which raises excitonic separation[108,109]. To find the best performance, the ETL layer's doping concentration is changed in this part from 1×10^{13} cm^{-3} to 1×10^{20} cm^{-3}. The output parameters of PSC, are also noted. At a resolution of 1×10^{17} cm^{-3}, the PSC exhibits optimal performance. It is also evident from Fig. 6a that there is no discernible change in V_{OC} or J_{SC} with the changing of N_D of ETL. Keeping the N_D in ETL to 1×10^{17} cm^{-3} initiates the subsequent assessment procedure and V_{OC}, J_{SC}, FF, and PCE are also nearly dramatically decreased. Similar features are noted in earlier published publications[7,110]. However, among all devices, the ZnSe ETL device comparatively shows better performance with a PCE, V_{OC}, J_{SC}, and FF of 21.05% 0.58 V, 43.94 mA/cm^2, and 82.17%, respectively.

Impact of defect density of ETL

For various ETLs, the values of V_{OC}, J_{SC}, FF, and PCE are calculated by raising the ETL defect density from 1×10^{12} cm^{-3} to 1×10^{18} cm^{-3}. As the N_t of the ETL increased, Fig. 6b demonstrated that practically all performance parameters—V_{OC}, J_{SC}, FF, and PCE—indicated quite constant values for all ETL layers except $PC_{60}BM$. When $PC_{60}BM$ is used as ETL all parameters V_{OC}, J_{SC}, FF, and PCE start to decrease when defect density is higher than 1×10^{16} cm^{-3}. PCE significantly decreases due to an increase in recombination pathways and trap states[111]. Therefore, a defect density of 1×10^{15} cm^{-3} can be considered optimal for better performance in all devices.

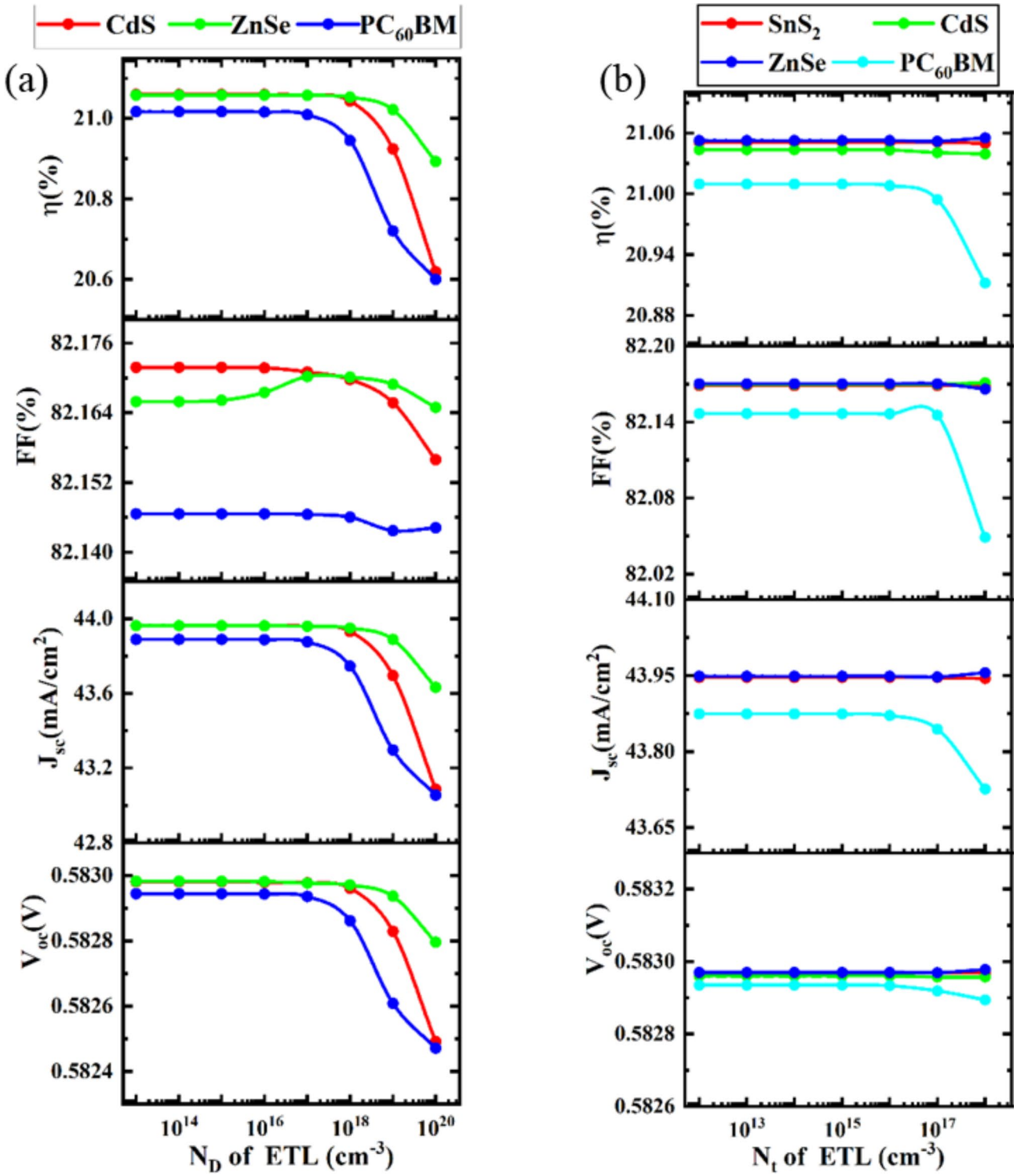

Fig. 6. Impact of donor and defect density of ETL on device performance.

However, the ZnSe ETL device achieves the highest V_{OC} value of 0.58 V, whereas the J_{SC} value of about 48.94 mA/cm^2. $PC_{60}BM$ as the ETL displayed a lower value of J_{SC} (43.87 mA/cm^2). The same characteristics are observed in previously reported articles[7,95,110].

Optimization of acceptor and defect density of HTL

Impact of acceptor density of HTL

Corresponding to ETL's donor density, the consequences of HTL's acceptor density increase the performance of PCSs. The process of separating the charge carriers generated by sunlight is largely dependent on the acceptor

concentration. HTL transfers holes to the anode. These charge carriers are distinguished by an electric field that depends on the acceptor density and is present at the absorber/ HTL contacts[108]. The acceptor density concentration throughout HTL sections can ameliorate the electric field at the interfaces. Consequently, when the acceptor density of HTL increases, fewer carriers recombine at the interfaces, resulting in a significant boost in excitonic separation and a reduction in minority carrier concentration[108,109].

The change in N_A of HTL from 1×10^{14} cm^{-3} to 1×10^{20} cm^{-3}, with all other optoelectronic parameters held constant, is shown in Fig. 7a. Up to 1×10^{16} cm^{-3} doping density, all the output parameters, such as V_{OC},

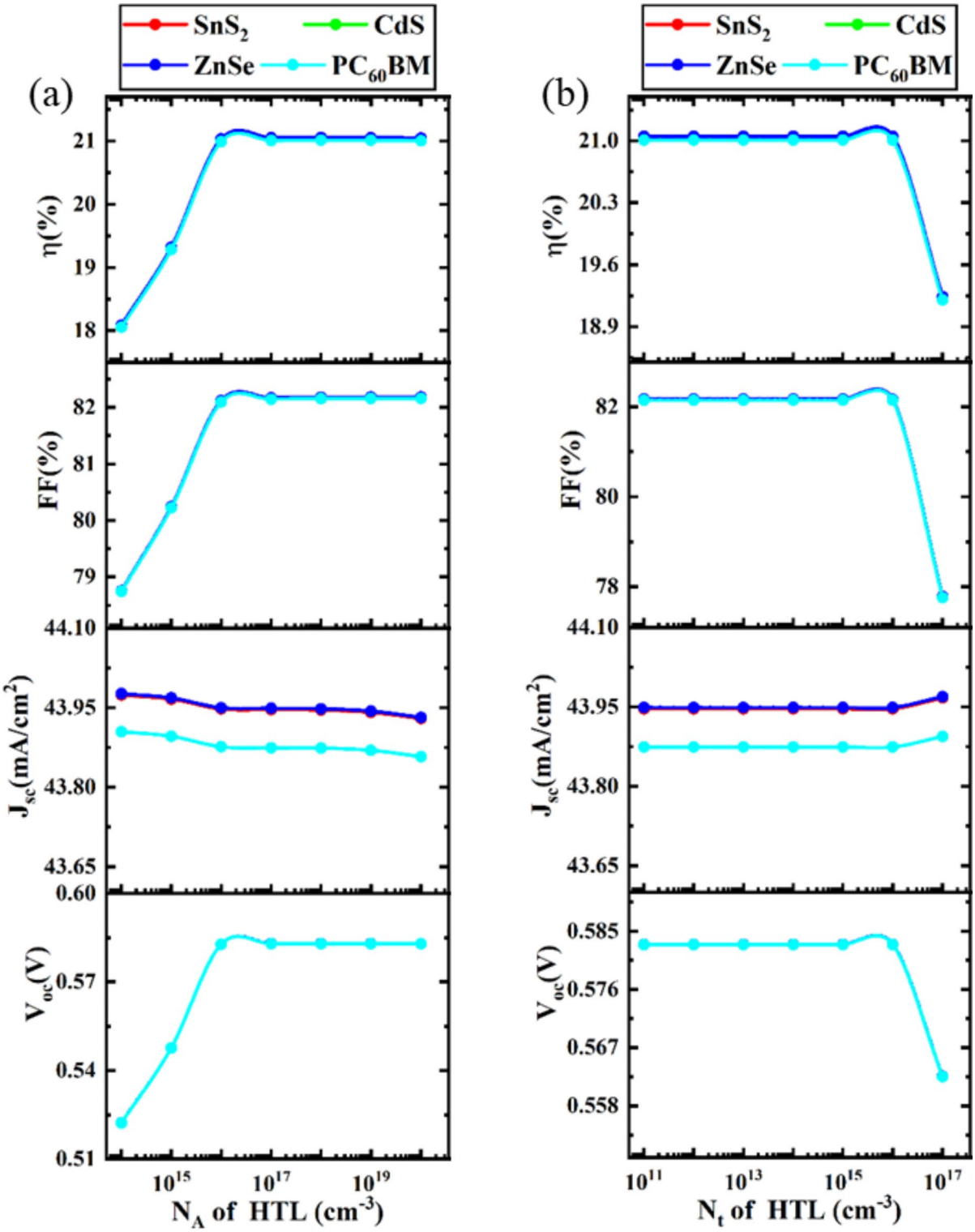

Fig. 7. Impact of acceptor and defect density of HTL on device performance.

FF, and PCE of PSC parameters start increasing while J_{SC} is constant. After increasing acceptor density 1×10^{16} cm^{-3}, V_{OC}, FF, and PCE remain constant. The optimal value for acceptor doping density is 1×10^{16} cm^{-3} since it exhibits the best PCE. By putting this optimization in place, an additional assessment procedure is carried out. Similar features are noted in earlier published publications[2,7,110].

Impact of defect density of HTL

The values of V_{OC}, J_{SC}, FF, and PCE are computed for different structures by increasing the HTL defect density from 1×10^{11} cm^{-3} to 1×10^{17} cm^{-3}. Figure 7b showed that almost all performance metrics (V_{OC}, J_{SC}, FF, and PCE) suggested nearly comparable characteristics for all structures when the N_t of the HTL rose. V_{OC}, FF, and PCE are practically constant up to 1×10^{16} cm^{-3} defect density; beyond that, they begin to drop, whereas J_{SC} is almost constant or all the density. V_{OC}, FF, and PCE begin to decline at an increase in acceptor density of 1×10^{16} cm^{-3}, although J_{SC} exhibits very little gain. The primary cause of this PCE deterioration is the rapid formation of numerous recombination sites within the HTL and at the interfaces after exceeding 1×10^{16} cm^{-3} of defect density[112]. This increased defect density in the HTL, caused by factors such as dislocations and native defects, leads to the formation of shallow traps. These traps negatively impact the cell's performance by acting as non-radiative recombination centers[113]. Given that it has the best PCE, 1×10^{16} cm^{-3} is the ideal acceptor doping density. By implementing this optimization, a further evaluation process is completed. Similar characteristics have been reported in past publications[7,95].

Effects of series resistance, shunt resistance, and temperature

Impact of series resistance on device performance

The combination of the absorber layer resistance and the ohmic contact resistance of the device is known as series resistance (R_S). The impact of varying the series resistance for four different ETLs (ZnSe, $PC_{60}BM$, ZnSe, and CdS)-associated structures from 0 Ω-cm^2 to 6 Ω-cm^2 is examined, as shown in Fig. 8a. It is shown that J_{SC} and V_{OC} were almost unaffected by increasing R_S. Nonetheless, the growth in R_S has resulted in an

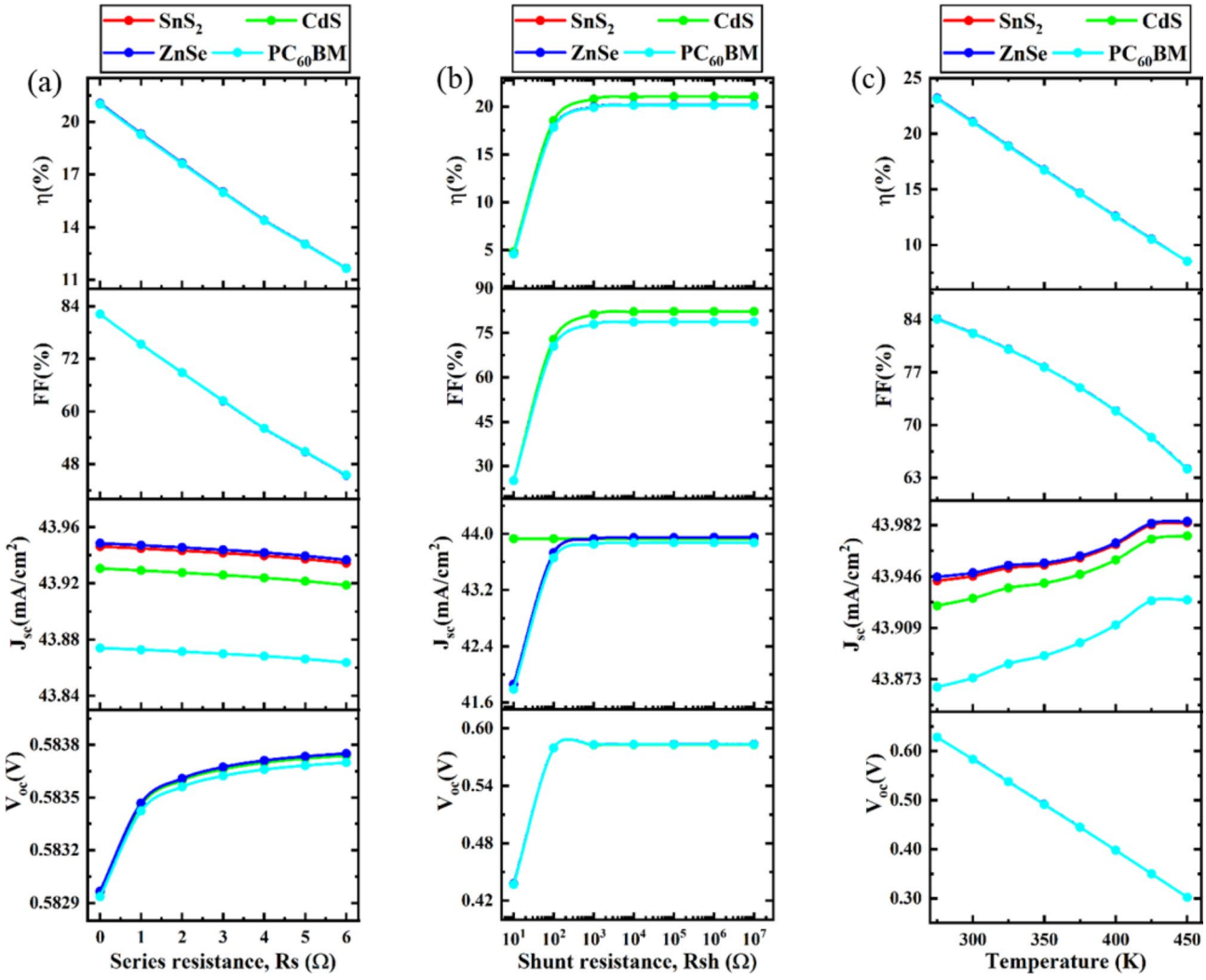

Fig. 8. Impact of series resistance, shunt resistance, and temperature on device performance.

enormous downturn in the FF (82–44%) and PCE (21–12%) for all structures. Consequently, throughout the device's manufacture, R_S must be reduced to a minimum to maximize performance and optimize FF. To reduce R_S, decreasing the thickness of the absorber layer during manufacturing is not a solution because of lowering the thickness of the absorber layer, as doing so causes a noncomplementary absorption[30,110]. Minimizing the resistance to contact between the electrodes and active layer or designing well-interacting donor-acceptor interfaces are two further experimental techniques to reduce R_S[30,110]. A similar output trend is noted in earlier published publications[114,115].

Impact of shunt resistance on device performance

Materials for absorbers, interface barriers, interlayers that gather charges, and electrodes all contribute to PSCs' internal resistance. The Shockley equation (Eqs. 13–14) describes how a solar cell's J-V characteristic responds under ideal one-sun illumination parameters[30,110,114].

$$J_{SC} = J_{PH} - J_o \left[\exp\left(\frac{q_e\,(V - JR_S)}{nKT_e}\right) - 1\right] - \frac{V - JR_S}{R_{Sh}} \tag{13}$$

.....

$$V_{OC} = \left(\frac{nKT_e}{q_e}\right) \ln\left[\frac{J_{PH}}{J_O}\left(1 - \frac{V_{OC}}{J_{PH}R_{Sh}}\right)\right] \tag{14}$$

.....

The equation includes the elementary charge (q_e), photocurrent density (J_{PH}), reverse bias saturation current density (J_o), series resistance (R_S), shunt resistance (R_{Sh}), diode ideality factor (n), Boltzmann constant (1.38×10^{23} JK^{-1}), and ambient temperature (298 K).

Figure 8b illustrates how V_{OC}, J_{SC}, FF, and PCE values affect R_{Sh} variation, which ranges from 10 Ω-cm[27] to 10 Ω-cm^2 for all PSC configurations. As R_{Sh} rose, the PV parameters followed a comparable pattern, rapidly rising from 10 Ω-cm[23] to 10 Ω-cm^2. According to Fig. 8b, different ETL-associated structures had the same V_{OC} of 0.58 V. Figure 8b shows that ZnSe, $PC_{60}BM$, ZnSe, and CdS as ETL structures, J_{SC} increased with the fluctuation of R_{Sh} for different ETL-associated structures. After 10^3 Ω-cm^2, the J_{SC} for R_{Sh} increased in all PSC structures and remained steady. As for FF, Fig. 8b indicates that all four PSC structures exhibited a rising trend; however, once R_{Sh} variation decreased, CdS, ETL-associated PSC structures, displayed about 80% FF. The remaining four PSC structures linked to ETLs exhibited less than 80% of FF. According to Fig. 8b, nearly the same trend was seen in the PCE cases of CdS, where the structure connected to the ETL has an enhanced PCE of about > 20%. A similar output trend is noted in earlier published publications[114,115]. Thus, this analysis indicates that maximizing shunt resistance is essential for achieving optimal device performance.

Impact of temperature on device performance

The power output of a PSC is directly impacted by its operating temperature. Higher operating temperatures are expected to have an impact on the density of states, band gaps, electron and hole mobility, carrier concentrations, and other solar cell properties[2]. Similarly, the operating temperature impacts the proposed cell's performance parameters. The temperature of this simulation impact is adjusted between 275 k and 450 K. Figure 8C displays the V_{OC} plotted against temperature fluctuation. The graph shows that when the working temperature of the cell rises, the V_{OC} falls, though J_{SC} remains almost constant. The creation of extra interfacial defects, a rise in series resistance, and a short carrier diffusion length may all be employed to clarify the decline in V_{OC} according to the operational temperature[2]. FF and PCE of the raised four models also start decreasing with an increment in temperature. According to our findings, the greatest PCE is produced under the usual test setting of 300 K, and the PCE declines linearly when the temperature escalates. The approximate PCE of the suggested cell at 300 K is 21.05% for the CdS- ETL-based PSC structure. The same phenomenon is noted in earlier published publications[116,117].

Effect of absorber layer thickness with absorber acceptor density

The absorber layer thickness and acceptor are critical factors impacting device performance. Optimizing these parameters is necessary to get optimal performance. During simulation, the absorber thickness was adjusted from 0.5 µm to 1.5 µm, and the N_A was modified from 1×10^{13} cm^{-3} to 1×10^{20} cm^{-3} to examine the effects of these factors on the PV performance characteristics of the four optimized PSCs. The impact of simultaneously varying the thickness of the absorber layer and N_A using contour plot mapping is seen in Fig. 9 on the PCE for the buildings under investigation. It is pleasing to note that when the thickness of the absorber was modified using absorber N_A, SnS_2, $PC_{60}BM$, ZnSe, and CdS ETL-based PSC structures displayed almost similar patterns. When both the NA and absorber thickness are less extensive than 1×10^{16} cm^{-3} and 0.95 µm, respectively, the maximum PCE (~21.05%) was observed in these four solar structures. Additionally, ZnSe and CdS as the ETL have the most prominent PCE among the four optimized PSCs, whereas $PC_{60}BM$ exhibits the lowest PCE. Therefore, it can be said that for $CsPb._{625}Zn._{375}IBr_2$ absorber-based PSCs, it is better to employ inorganic oxide-based ETLs rather than organic ones.

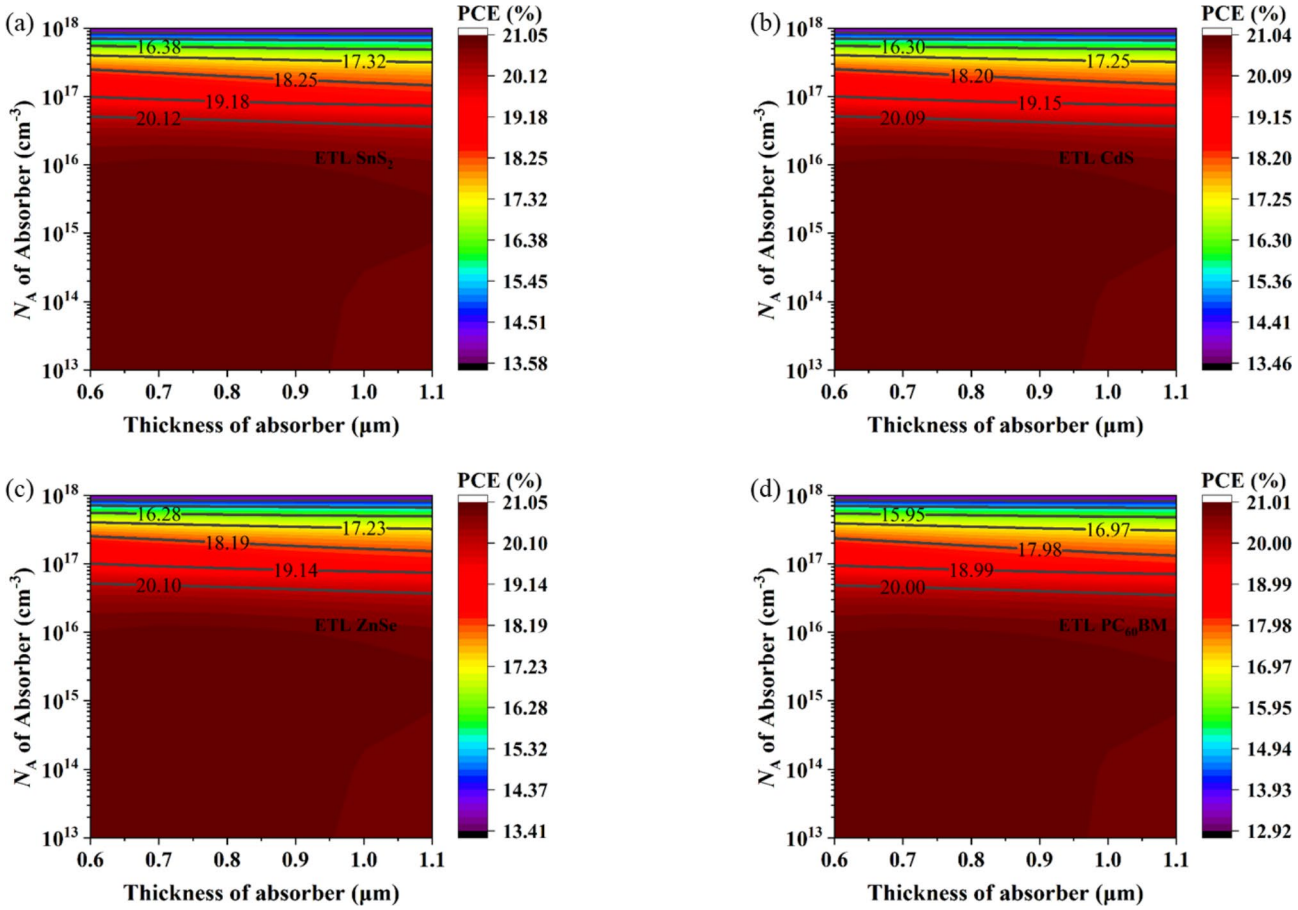

Fig. 9. Correlation between absorber acceptor density and absorber layer thickness.

Effect of absorber layer thickness with absorber donor density

This work uses contour mapping to examine how adjusting the absorber donor density and width of the absorber layer affects the performance of the $CsPb._{625}Zn._{375}IBr_2$ absorber-based PSCs. When N_D is less than 1×10^{16} cm^{-3} and the absorber thickness is 0.6 µm to 1.1 µm, the PCE is at its highest (> 21%). When N_D rises more than 1×10^{16} cm^{-3}, PCE starts to fall as well, but absorber layer thickness has no impact on PCE. As Fig. 10 shows, the maximum value of PCE (21.07%) can be obtained using SnS_2 and ZnSe ETL-based PSC structures whereas $PC_{60}BM$ exhibits the lowest PCE. Therefore, it can be said that for $CsPb._{625}Zn._{375}IBr_2$ absorber-based PSCs, it is better to employ inorganic oxide-based ETLs rather than organic ones.

Effect of absorber layer thickness with absorber defect density

The absorber thickness and defect density have a major direct impact on the Solar cell performance. Increased recombination lowers the PCE of PSCs because greater N_t in the absorber layer causes pinhole formation and film breakdown[30,110]. By adjusting the absorber depth between 0.6 µm and 1.1 µm, the simulation was run to determine the most beneficial defect density for a given absorber layer thickness and N_t adjusted between 1×10^{11} cm^{-3} to 1×10^{16} cm^{-3}. For every building under investigation, Fig. 11 shows variations in absorber layer thickness and N_t, which cause PCE to fluctuate. Figure 11 illustrates how variations in absorber thickness and N_t affect PCE. As ETL-based solar structures, SnS_2, $PC_{60}BM$, ZnSe, and CdS exhibit a comparable pattern for the PCE value with adjustments to N_t and absorber thickness, as shown in Fig. 11. Out of all the devices under study, SnS_2 and ZnSe, as the ETL demonstrated the maximum PCE of around 21.05% happens when the absorber depth ranges from 0.6 µm to 1.1 µm and defect density, is less than 2×10^{13} cm^{-3}. In the presence of a defect, inorganic ETLs (SnS_2, ZnSe, and CdS) based PSCs outperform the organic ETLs-based PSCs.

Effect of generation rate and recombination rate

The coupling and annihilation of electrons and holes in the conduction band is the process of recombination. The lifespan and charge carrier density both have an impact on the recombination rate. Furthermore, the electron-hole recombination is affected by every defect condition present in the several PSC layers[95]. The four PSCs had a maximum recombination rate that was like the generation rate, within 1.0 µm, as seen in Fig. 12a. The region between 1.0 µm displayed an elevated recombination rate due to more conduction band electrons crossing the energy barrier, entering the valence band, and becoming more stable by taking the position of the valence band hole. The consequence of energy levels influences the electron hole's recombination rate inside the device, and

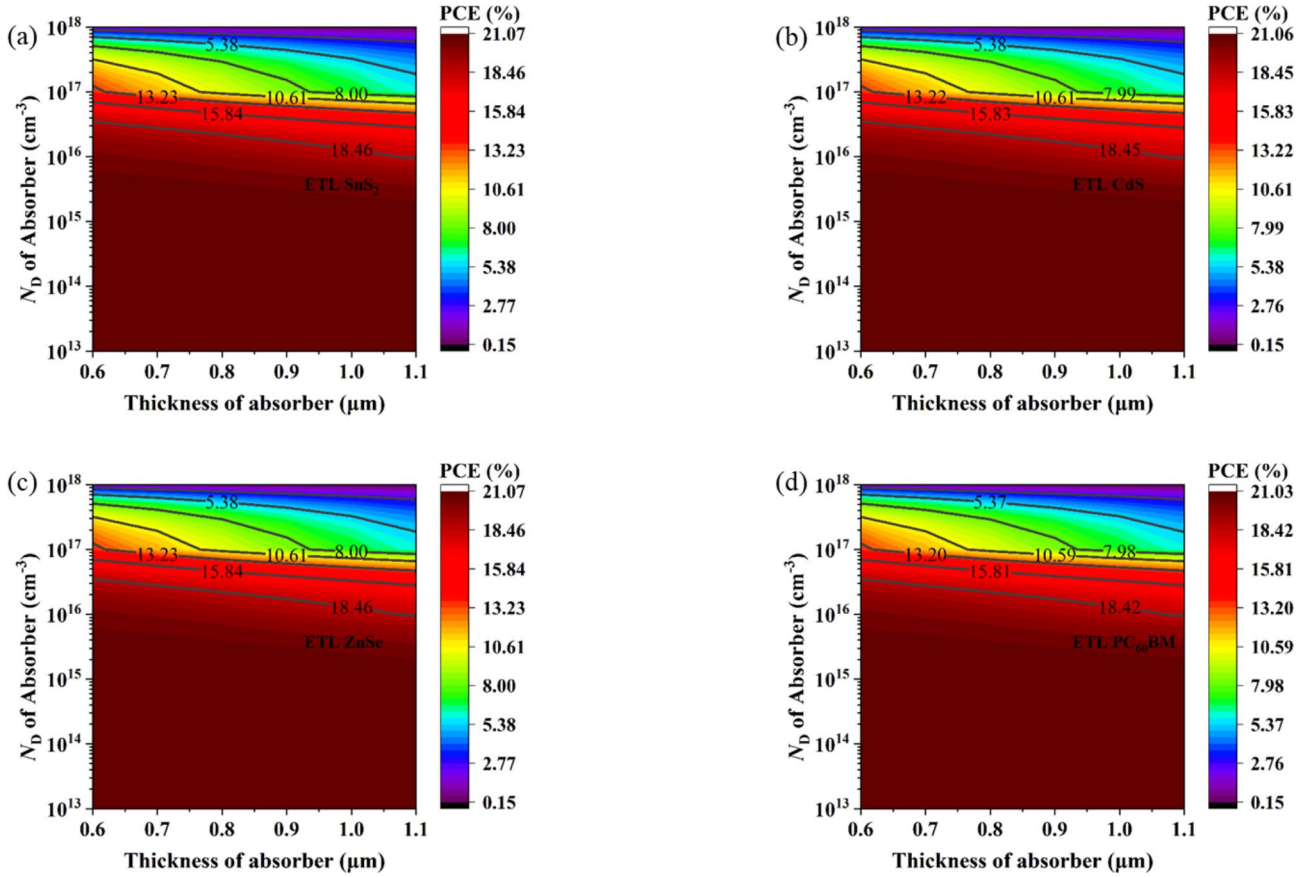

Fig. 10. Effect of absorber layer thickness with absorber donor density.

imperfection and grain boundaries may cause the recombination rate distribution in the solar architecture to be non-uniform[95].

The generated electron-hole pair may be found for any wavelength of light, the whole conventional solar spectrum, and at any position within the solar cell. The largest generation rate is near the device surface, where most of the light is absorbed[30,110]. The generation rate of a solar cell indicates the quantity of electron-hole pairs produced inside the device as a result of photon absorption at a certain wavelength., which depends on both position and wavelength. The generation rate is essential for PSCs to operate as efficiently as possible. The four optimized solar devices' generating rates are displayed in Fig. 12b. As the figure makes clear, all four different structure PSCs based on SnS_2, ZnSe, $PC_{60}BM$, and CdS ETLs demonstrated generation rates start increasing from 0.2 μm and reached greater generation rate at PSC depths of 1.0 μm.

JV and QE characteristics curve

The quantity of current produced by photoirradiation at a certain wavelength is known as a perovskite solar cell's quantum efficiency (QE)[118,119]. The number of charge carriers that are moved and gathered by the electrodes can also be used to calculate the QE. The ideal form of a solar cell's QE curve is square or rectangular; however, it can be distorted by factors such as surface passivation, recombination, and reflection losses[49,103]. For the solar cell architectures of FTO/SnS_2/$CsPb._{625}Zn._{375}IBr_2$/$MoS_2$/Au, FTO/ZnSe/$CsPb._{625}Zn._{375}IBr_2$/$MoS_2$/Au, FTO/CdS/$CsPb._{625}Zn._{375}IBr_2$/$MoS_2$/Au and FTO/$PC_{60}BM$/$CsPb._{625}Zn._{375}IBr_2$/$MoS_2$/Au, the nature of QE for varying wavelength is investigated to more precisely recognize the accumulation of charge carriers. The QE curves for both solar cell architectures are displayed in Fig. 13a before the optimization condition. Figure 13a illustrates that all four structures have a QE of 100% at 400 nm. However, QE begins to decline after 1000 nm wavelength in all cases of structures. The QE graph is square and deemed excellent when the QE value remains constant over the observed wavelength range. The QE of the PSC is lowered due to the recombination, even if the charge carriers cannot go into an external circuit. For most solar cells, recombination lowers QE while charge carriers are incapable of an external circuit. The same factors that affect collection probability also affect QE. Modifying the front surface, for instance, may affect carriers formed close to the surface. Longer wavelength QE can be decreased by the absorbance of free carriers from front surface layers that are highly doped.

The J-V characteristic curve of the PSCs architectures including FTO/SnS_2/$CsPb._{625}Zn._{375}IBr_2$/$MoS_2$/Au, FTO/ZnSe/$CsPb._{625}Zn._{375}IBr_2$/$MoS_2$/Au, FTO/CdS/$CsPb._{625}Zn._{375}IBr_2$/$MoS_2$/Au and FTO/$PC_{60}BM$/$CsPb._{625}Zn._{375}IBr_2$/$MoS_2$/Au are shown in Fig. 13b. As seen in Fig. 13b, all four PSC structures displayed a J_{SC} of about 44 mA/cm^2 when the V_{OC} was around 0.58 V. Defect states in perovskite films led to a considerable drop

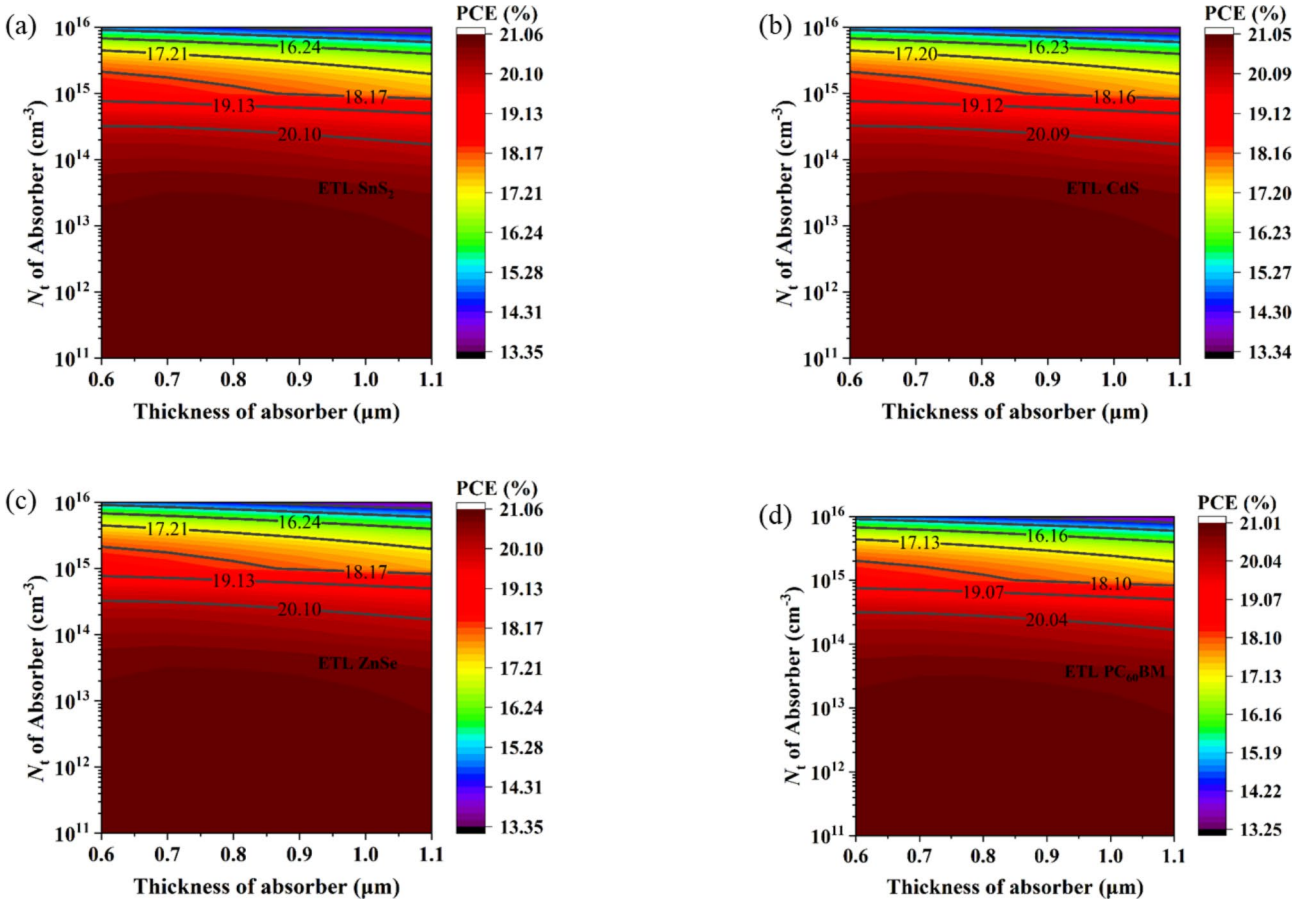

Fig. 11. Effect of absorber layer thickness with absorber defect density.

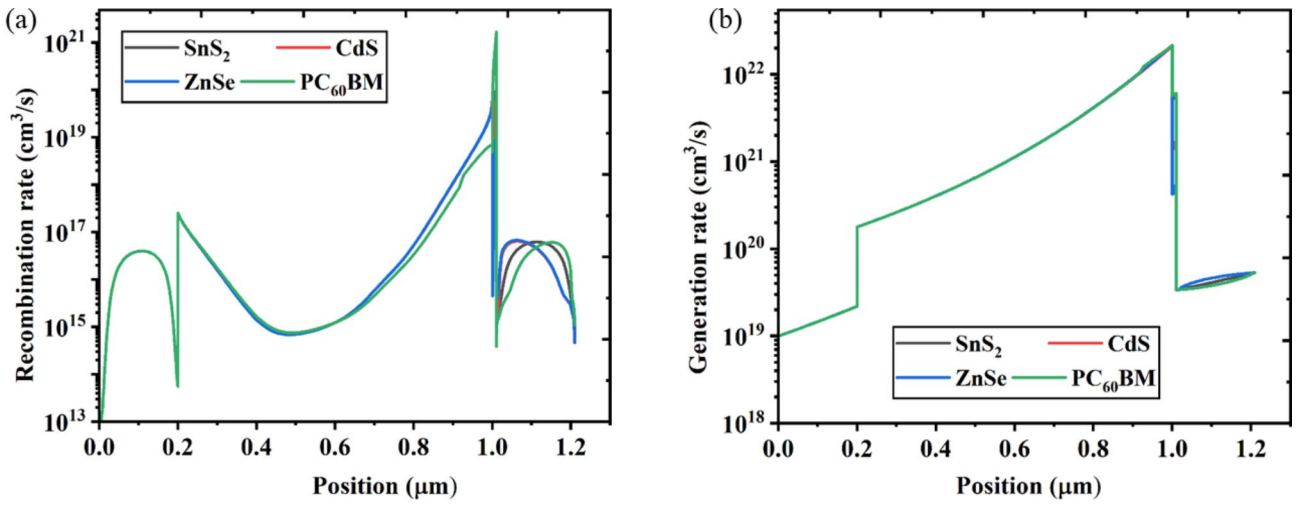

Fig. 12. Effect of generation rate and recombination rate.

in all photovoltaic metrics. This is in line with studies showing that perovskite's notable crystallization improves its functioning and diminishes charge recombination.

Conclusion

This work thoroughly examines several $CsPb._{625}Zn._{375}IBr_2$ -based PSC features with varying HTLs and ETLs. Through an examination of key variables influencing PSC performance, the study seeks to identify the optimal

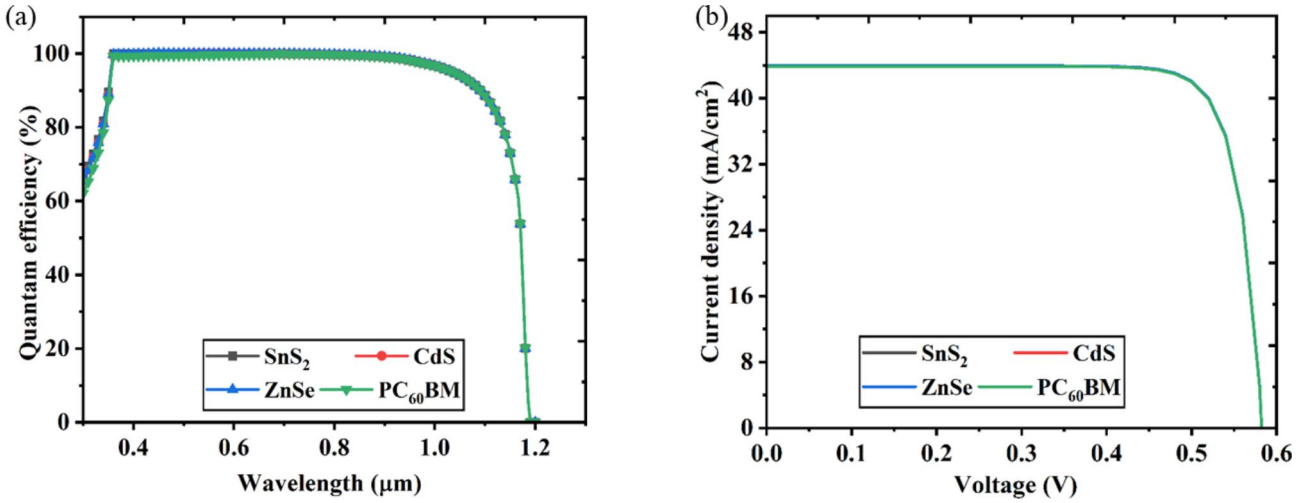

Fig. 13. JV and QE characteristics curve.

design for maximizing conversion efficiency. According to the study, the following elements are crucial for maximizing PSC performance:

1. First of all, we analyzed different types of HTL materials for $CsPb._{625}Zn._{375}IBr_2$ -based PSC, and the best HTL materials for $CsPb._{625}Zn._{375}IBr_2$ -based PSC is MoS_2.

2. Device performance is significantly impacted by the thickness of the absorber, ETL, and HTL. We found that 800 nm thick absorber layer, 100 nm thick ETL layer, and 50 nm thick HTL layer help us to get the best result.

3. To get the optimum performance we need to set both the acceptor density and donor density of the absorber to less than 1×10^{16} cm^{-3} and defect density should not be higher than 1×10^{14} cm^{-3}.

4. The density of HTL acceptors and ETL donors should be less than 1×10^{17} cm^{-3} and the defect density should be less than 1×10^{15} cm^{-3}.

5. Shunt resistance enhances PCE and FF and has negligible effects on J_{SC} and V_{OC}, while an increase in series resistance drastically reduces PCE.

In summary, our thorough analysis shows that several factors, including properties of the ETL and HTL, the width of the absorber layer, acceptor density, and defect densities, influence the performance of $CsPb._{625}Zn._{375}IBr_2$ -based PSCs. By optimizing these parameters, PCEs of 21.05% for the FTO/ZnSe/$CsPb._{625}Zn._{375}IBr_2$/$MoS_2$/Au structures and 21.04% for the FTO/CdS/$CsPb._{625}Zn._{375}IBr_2$/$MoS_2$/Au structures are obtained. By laying the groundwork for future improvements in stability and efficiency, these optimized designs prepare the ground for using $CsPb._{625}Zn._{375}IBr_2$ -based PSCs in renewable energy applications.

Data availability

The datasets used and/or analysed during the current study available from the corresponding author on reasonable request.

Received: 28 August 2024; Accepted: 29 November 2024
Published online: 03 December 2024

References

1. Kang, J. & Cho, J. H. Organic-inorganic hybrid perovskite electronics. *Phys. Chem. Chem. Phys.* **22**, 13347–13357 (2020).
2. Chakrabartty, J., Islam, M. A. & Reza, S. Performance analysis of highly efficient 2D/3D bilayer inverted perovskite solar cells. *Sol Energy*. **230**, 195–207 (2021).
3. Hossain, M. K. et al. Exploring the optoelectronic and photovoltaic characteristics of lead-free Cs_2TiBr_6 double perovskite solar cells: a DFT and SCAPS-1D investigations. *Adv. Electron. Mater.* https://doi.org/10.1002/aelm.202400348 (2024).
4. Hossain, M. K. et al. Design insights into La_2NiMnO_6-based perovskite solar cells employing different charge transport layers: DFT and SCAPS-1D frameworks. *Energy Fuels*. **37**, 13377–13396 (2023).
5. Roy, P., Kumar Sinha, N., Tiwari, S. & Khare, A. A review on perovskite solar cells: evolution of architecture, fabrication techniques, commercialization issues and status. *Sol Energy*. **198**, 665–688 (2020).
6. Tailor, N. K. et al. Recent progress in morphology optimization in perovskite solar cell. *J. Mater. Chem. A* **8**, 21356–21386 https://doi.org/10.1039/d0ta00143k (2020).
7. Hossain, M. K. et al. High-efficiency lead-free La_2NiMnO_6-based double perovskite solar cell by incorporating charge transport layers composed of WS_2, ZnO, and Cu_2FeSnS_4. *Energy Fuels*. **37**, 19898–19914 (2023).
8. Uddin, M. S. et al. An in-depth investigation of the combined optoelectronic and photovoltaic properties of lead-free $Cs_2AgBiBr_6$ double perovskite solar cells using DFT and SCAPS-1D frameworks. *Adv. Electron. Mater.* **10**, 2300751 (2024).
9. A, K. et al. Organometal halide perovskites as visible-light sensitizers for photovoltaic cells. *J. Am. Chem. Soc.* **131**, 6050–6051 (2009).
10. NREL. Best Research-Cell Efficiency Chart | Photovoltaic Research | NREL. (2023).
11. Hossain, M. K. et al. An extensive study on charge transport layers to design and optimization of high-efficiency lead-free Cs_2PtI_6-based double-perovskite solar cells: a numerical simulation approach. *Results Phys.* **61**, 107751 (2024).

12. Grancini, G. & Nazeeruddin, M. K. Dimensional tailoring of hybrid perovskites for photovoltaics. *Nat. Rev. Mater.* 4, 4–22 https://doi.org/10.1038/s41578-018-0065-0 (2019).
13. Chakrabartty, J., Harnagea, C., Celikin, M., Rosei, F. & Nechache, R. Improved photovoltaic performance from inorganic perovskite oxide thin films with mixed crystal phases. *Nat. Photonics*. **12**, 271–276 (2018).
14. Song, Z. et al. Perovskite solar cell stability in humid air: partially reversible phase transitions in the PbI 2 -CH 3 NH 3 I-H 2 O system. *Adv. Energy Mater.* **6**, 1600846 (2016).
15. Tiep, N. H., Ku, Z. & Fan, H. J. Recent advances in improving the stability of perovskite solar cells. *Adv. Energy Mater.* **6**, (2016).
16. Salhi, B., Wudil, Y. S., Hossain, M. K., Al-Ahmed, A. & Al-Sulaiman, F. A. Review of recent developments and persistent challenges in stability of perovskite solar cells. *Renew. Sustain. Energy Rev.* 90, 210–222 https://doi.org/10.1016/j.rser.2018.03.058 (2018).
17. Wang, R. et al. A review of perovskites solar cell stability. *Adv. Funct. Mater.* **29**, 1808843 (2019).
18. Ortiz-Cervantes, C., Carmona-Monroy, P. & Solis-Ibarra, D. Two-dimensional halide perovskites in solar cells: 2D or not 2D? *ChemSusChem* **12**, 1560–1575 https://doi.org/10.1002/cssc.201802992 (2019).
19. Yan, J., Qiu, W., Wu, G., Heremans, P. & Chen, H. Recent progress in 2D/quasi-2D layered metal halide perovskites for solar cells. *Journal of Materials Chemistry A* **6**, 11063–11077 https://doi.org/10.1039/c8ta02288g (2018).
20. Tai, Q., Tang, K. C. & Yan, F. Recent progress of inorganic perovskite solar cells. *Energy Environ. Sci.* **12**, 2375–2405 https://doi.org/10.1039/c9ee01479a (2019).
21. Ma, C. et al. 2D/3D perovskite hybrids as moisture-tolerant and efficient light absorbers for solar cells. *Nanoscale* **8**, 18309–18314 (2016).
22. Duan, J. et al. Inorganic perovskite solar cells: an emerging member of the photovoltaic community. *J. Mater. Chem. A*. **7**, 21036–21068 (2019).
23. Wang, J. et al. Highly efficient all-inorganic perovskite solar cells with suppressed non-radiative recombination by a Lewis base. *Nat. Commun.* **11**, 177 (2020).
24. Liu, X. et al. Boosting the efficiency of carbon-based planar CsPbBr3 perovskite solar cells by a modified multistep spin-coating technique and interface engineering. *Nano Energy*. **56**, 184–195 (2019).
25. Zhang, J., Hodes, G., Jin, Z. & Liu, S. All-inorganic CsPbX3 perovskite solar cells: progress and prospects. *Angewandte Chemie - International Edition* **58**, 15596–15618 https://doi.org/10.1002/anie.201901081 (2019).
26. Zeng, Q. et al. Inorganic CsPbI2Br perovskite solar cells: the progress and perspective. *Sol RRL* **3**, (2019).
27. Yuan, Y., Yan, G., Hong, R., Liang, Z. & Kirchartz, T. Quantifying efficiency limitations in all-inorganic halide perovskite solar cells. *Adv. Mater.* **34** https://doi.org/10.1002/adma.202108132 (2022).
28. Maafa, I. M. All-Inorganic perovskite solar cells: recent advancements and challenges. *Nanomaterials* **12** https://doi.org/10.3390/nano12101651 (2022).
29. Chen, H. et al. Inorganic perovskite solar cells: a rapidly growing field. *Solar RRL* **2** https://doi.org/10.1002/solr.201700188 (2018).
30. Hossain, M. K. et al. Numerical Analysis in DFT and SCAPS-1D on the influence of different charge transport layers of $CsPbBr_3$ perovskite solar cells. *Energy Fuels*. **37**, 6078–6098 (2023).
31. Kaur, N. et al. Low lead inorganic Zn-based mixed-halide perovskites $CsPb_{0.625}Zn_{0.375}I_{3-\beta}X_{\beta}$ (X = cl or br) for energy generation with 23.5% efficiency. *Phys. Scr.* **98**, 115941 (2023).
32. Kaur, N., Madan, J. & Pandey, R. Numerical simulation study of CsPb0.625Zn0.375IBr2 perovskite solar cell. *Mater. Today Proc.* https://doi.org/10.1016/j.matpr.2023.03.367 (2023).
33. Lee, S. et al. Inorganic narrow bandgap CsPb0.4Sn0.6I2.4Br0.6 perovskite solar cells with exceptional efficiency. *Nano Energy*. **77**, 105309 (2020).
34. Liang, J. et al. CsPb0.9Sn0.1IBr2 based all-inorganic perovskite solar cells with exceptional efficiency and stability. *J. Am. Chem. Soc.* **139**, 14009–14012 (2017).
35. Yang, F. et al. All-inorganic CsPb1 – GeI2Br perovskite with enhanced phase stability and photovoltaic performance. *Angew Chemie Int. Ed.* **57**, 12745–12749 (2018).
36. Li, N., Zhu, Z., Li, J., Jen, A. K. Y. & Wang, L. Inorganic CsPb1 – SnIBr2 for efficient wide-bandgap perovskite solar cells. *Adv. Energy Mater.* **8**, 1800525 (2018).
37. Yaghoobi Nia, N. et al. Impact of P3HT regioregularity and molecular weight on the efficiency and stability of perovskite solar cells. *ACS Sustain. Chem. Eng.* **9**, 5061–5073 (2021).
38. Salim, T. et al. Perovskite-based solar cells: impact of morphology and device architecture on device performance. *J. Mater. Chem. A*. **3**, 8943–8969 (2015).
39. Diau, E. W. G., Jokar, E. & Rameez, M. Strategies to improve performance and stability for tin-based perovskite solar cells. *ACS Energy Lett.* **4**, 1930–1937 https://doi.org/10.1021/acsenergylett.9b01179 (2019).
40. Pascual, J. et al. Lights and shadows of DMSO as solvent for tin halide perovskites. *Chem. – Eur. J.* **28**, e202103919 (2022).
41. Aygan Atesin Sajid Bashir Jingbo Louise Liu & Editors, T. *Nanostructured Materials for Next-Generation Energy Storage and Conversion* https://doi.org/10.1007/978-3-662-59594-7 (Springer, 2019).
42. Ghosh, R., Singh, A. & Agarwal, P. Study on effect of different HTL and ETL materials on the perovskite solar cell performance with TCAD simulator. *Mater. Today Proc.* https://doi.org/10.1016/J.MATPR.2023.06.161 (2023).
43. Bichave, S., Mundupuzhakal, J., Gajjar, P. N. & Gupta, S. K. Analysis of varying ETL/HTL material for an effective perovskite solar cell by numerical simulation. *Mater. Today Proc.* https://doi.org/10.1016/J.MATPR.2023.01.190 (2023).
44. Jamal, S., Khan, A. D. & Khan, A. D. High performance perovskite solar cell based on efficient materials for electron and hole transport layers. *Optik (Stuttg)* **218**, (2020).
45. Fatema, K. & Arefin, M. S. Enhancing the efficiency of Pb-based and Sn-based perovskite solar cell by applying different ETL and HTL using SCAPS-ID. *Opt. Mater. (Amst).* **125**, 112036 (2022).
46. Prochowicz, D. et al. Suppressing recombination in perovskite solar cells via surface engineering of TiO_2 ETL. *Sol Energy*. **197**, 50–57 (2020).
47. Tavakoli, M. M., Yadav, P., Tavakoli, R. & Kong, J. Surface engineering of TiO_2 ETL for highly efficient and hysteresis-less planar perovskite solar cell (21.4%) with enhanced open-circuit voltage and stability. *Adv. Energy Mater.* **8**, (2018).
48. Lin, L. et al. Inorganic electron transport materials in perovskite solar cells. *Adv. Funct. Mater.* **31** https://doi.org/10.1002/adfm.202008300 (2021).
49. Rai, N., Rai, S., Singh, P. K., Lohia, P. & Dwivedi, D. K. Analysis of various ETL materials for an efficient perovskite solar cell by numerical simulation. *J. Mater. Sci. Mater. Electron.* **31**, 16269–16280 (2020).
50. Abulikemu, M., Barbé, J., Labban, E., Eid, A., Del Gobbo, S. & J. & Planar heterojunction perovskite solar cell based on CdS electron transport layer. *Thin Solid Films*. **636**, 512–518 (2017).
51. Patil, P. et al. Hybrid interfacial ETL engineering using PCBM-SnS2 for high-performance p-i-n structured planar perovskite solar cells. *Chem. Eng. J.* **397**, 125504 (2020).
52. Benali, H. et al. Synthesis and characterization of Mg-doped ZnO thin-films for photovoltaic applications. *Mater. Today Proc.* **66**, 212–216 (2022).
53. Li, X. et al. Thermally evaporated ZnSe for efficient and stable regular/inverted perovskite solar cells by enhanced electron extraction. *ENERGY Environ. Mater.* **6**, e12439 (2023).
54. Namkoong, G., Mamun, A. A. & Ava, T. T. Impact of PCBM/C60 electron transfer layer on charge transports on ordered and disordered perovskite phases and hysteresis-free perovskite solar cells. *Org. Electron.* **56**, 163–169 (2018).

55. Li, S., Cao, Y. L. Y. L., Li, W. H. W. H. & Bo, Z. S. Z. S. A brief review of hole transporting materials commonly used in perovskite solar cells. *Rare Met.* **40**, 2712–2729 (2021).
56. Pitchaiya, S. et al. A review on the classification of organic/inorganic/carbonaceous hole transporting materials for perovskite solar cell application. *Arab. J. Chem.* **13**, 2526–2557 https://doi.org/10.1016/j.arabjc.2018.06.006 (2020).
57. Shariatinia, Z. Recent progress in development of diverse kinds of hole transport materials for the perovskite solar cells: A review. *Renew. Sustain. Energy Rev.* **119** https://doi.org/10.1016/j.rser.2019.109608 (2020).
58. Murugan, P., Hu, T., Hu, X. & Chen, Y. Advancements in organic small molecule holetransporting materials for perovskite solar cells: Past and future. *J. Mater. Chem. A* 10, 5044–5081 https://doi.org/10.1039/d1ta11039j (2022).
59. Wang, J. M. et al. Small molecule-polymer composite hole-transporting layer for highly efficient and stable perovskite solar cells. *ACS Appl. Mater. Interfaces.* **9**, 13240–13246 (2017).
60. Vasilopoulou, M. et al. Molecular materials as interfacial layers and additives in perovskite solar cells. *Chem. Soc. Rev.* **49**, 4496–4526 https://doi.org/10.1039/c9cs00733d (2020).
61. Elseman, A. M., Sajid, S., Shalan, A. E., Mohamed, S. A. & Rashad, M. M. Recent progress concerning inorganic hole transport layers for efficient perovskite solar cells. *Appl. Phys. A Mater. Sci. Process.* **125** https://doi.org/10.1007/s00339-019-2766-7 (2019).
62. Arumugam, G. M. et al. Inorganic hole transport layers in inverted perovskite solar cells: a review. *Nano Sel.* **2**, 1081–1116 (2021).
63. Kung, P. K. et al. A review of inorganic hole transport materials for perovskite solar cells. *Adv. Mater. Interfaces.* **5** https://doi.org/10.1002/admi.201800882 (2018).
64. Hossain, M. K. et al. Enhancing efficiency and performance of Cs_2TiI_6-based perovskite solar cells through extensive optimization: a numerical approach. *Inorg. Chem. Commun.* **168**, 112964 (2024).
65. Et-taya, L., Ouslimane, T. & Benami, A. Numerical analysis of earth-abundant Cu2ZnSn(SxSe1-x)4 solar cells based on spectroscopic ellipsometry results by using SCAPS-1D. *Sol Energy.* **201**, 827–835 (2020).
66. Hossain, M. K. et al. Influence of natural dye adsorption on the structural, morphological and optical properties of TiO_2 based photoanode of dye-sensitized solar cell. *Mater. Sci.* **36**, 93–101 (2017).
67. Hossain, M. K., Rahman, M. T., Basher, M. K., Manir, M. S. & Bashar, M. S. Influence of thickness variation of gamma-irradiated DSSC photoanodic TiO_2 film on structural, morphological and optical properties. *Optik (Stuttg).* **178**, 449–460 (2019).
68. Hossain, M. K. et al. Efficiency enhancement of natural dye sensitized solar cell by optimizing electrode fabrication parameters. *Mater. Sci.* **35**, 816–823 (2017).
69. Hossain, M. K., Rahman, M. T., Basher, M. K., Afzal, M. J. & Bashar, M. S. Impact of ionizing radiation doses on nanocrystalline TiO_2 layer in DSSC's photoanode film. *Results Phys.* **11**, 1172–1181 (2018).
70. Rani, S., Kumar, A. & Ghosh, D. S. Optical designing of perovskite solar cells. https://doi.org/10.1109/JPHOTOV.2022.3141344 (2022).
71. Rani, S., Kumar, A. & Sundar Ghosh, D. High performance of NiO-Ag-NiO based semi-transparent perovskite solar cell. *Mater. Today Proc.* **66**, 3224–3227 (2022).
72. Basher, M. K., Hossain, M. K., Uddin, M. J., Akand, M. A. R. & Shorowordi, K. M. Effect of pyramidal texturization on the optical surface reflectance of monocrystalline photovoltaic silicon wafers. *Optik (Stuttg).* **172**, 801–811 (2018).
73. Hossain, M. I. et al. Effect of back reflectors on photon absorption in thin-film amorphous silicon solar cells. *Appl. Nanosci.* **7**, 489–497 (2017).
74. Basher, M. K. et al. Study and analysis the Cu nanoparticle assisted texturization forming low reflective silicon surface for solar cell application. *AIP Adv.* **9**, 1–6 (2019).
75. Basher, M. K., Hossain, M. K. & Akand, M. A. R. Effect of surface texturization on minority carrier lifetime and photovoltaic performance of monocrystalline silicon solar cell. *Optik (Stuttg).* **176**, 93–101 (2019).
76. Singh, N., Agarwal, A. & Agarwal, M. Performance evaluation of lead–free double-perovskite solar cell. *Opt. Mater. (Amst).* **114**, 110964 (2021).
77. Singh, N. K., Agarwal, A. & Kanumuri, T. Performance enhancement of environmental friendly ge-based perovskite solar cell with zn 3 P 2 and SnS 2 as charge transport layer materials. *Energy Technol.* **10**, 2100782 (2022).
78. Bansal, S. & Aryal, P. Evaluation of new materials for electron and hole transport layers in perovskite-based solar cells through SCAPS-1D simulations. In *Conf. Rec. IEEE Photovolt. Spec. Conf.* 747–750 (2016).
79. Raza, E. et al. Numerical simulation analysis towards the effect of charge transport layers electrical properties on cesium based ternary cation perovskite solar cells performance. *Sol Energy.* **225**, 842–850 (2021).
80. Qasim, I. et al. Numerical optimization of (FTO/ZnO/CdS/CH3NH3SnI3/GaAs/Au) perovskite solar cell using solar capacitance simulator with efficiency above 23% predicted. *Opt. Quantum Electron.* **53**, 713 (2021).
81. Singh, N. K. & Agarwal, A. Performance assessment of sustainable highly efficient CsSn0.5Ge0.5I3/FASnI3 based perovskite solar cell: a numerical modelling approach. *Opt. Mater. (Amst).* **139**, 113822 (2023).
82. Khan, Z., Noman, M., Tariq Jan, S. & Daud Khan, A. Systematic investigation of the impact of kesterite and zinc based charge transport layers on the device performance and optoelectronic properties of ecofriendly tin (sn) based perovskite solar cells. *Sol Energy.* **257**, 58–87 (2023).
83. Shamna, M. S. & Sudheer, K. S. Device modeling of Cs2PtI6-based perovskite solar cell with diverse transport materials and contact metal electrodes: a comprehensive simulation study using solar cell capacitance simulator. *J. Photonics Energy.* **12**, 1–17 (2022).
84. Karimi, E. & Ghorashi, S. M. B. Investigation of the influence of different hole-transporting materials on the performance of perovskite solar cells. *Optik (Stuttg).* **130**, 650–658 (2017).
85. Kaity, A., Shubham, Singh, S. & Pandey, S. K. Optimal design and photovoltaic performance of eco friendly, stable and efficient perovskite solar cell. *Superlattices Microstruct.* **156**, 106972 (2021).
86. Singh, N. K. & Agarwal, A. Numerical investigation of electron/hole transport layer for enhancement of ecofriendly Tin-Ge based perovskite solar cell. *Energy Sources Part. Recover Util. Environ. Eff.* **45**, 3087–3106 (2023).
87. AlZoubi, T., Mourched, B., Al Gharram, M. & Makhadmeh, G. & Abu Noqta, O. improving photovoltaic performance of hybrid organic-inorganic MAGeI3 perovskite solar cells via numerical optimization of carrier transport materials (HTLs/ETLs). *Nanomaterials* **13** (2023).
88. Minemoto, T. & Murata, M. Theoretical analysis on effect of band offsets in perovskite solar cells. *Sol Energy Mater. Sol Cells.* **133**, 8–14 (2015).
89. Pindolia, G. & Shinde, S. M. Effect of phthalocyanine-based charge transport layers on unleaded KSnI 3 perovskite solar cell. *Phys. Scr.* **98**, 065520 (2023).
90. Pindolia, G. & Shinde, S. M. Prediction of efficiency for KSnI3 perovskite solar cells using supervised machine learning algorithms. *J. Electron. Mater.* **53**, 3268–3275 (2024).
91. Hossain, M. K. et al. Combined DFT, SCAPS-1D, and wxAMPS frameworks for design optimization of efficient Cs_2BiAgI_6-based perovskite solar cells with different charge transport layers. *RSC Adv.* **12**, 34850–34873 (2022).
92. Jan, S. T. & Noman, M. Analyzing the effect of planar and inverted structure architecture on the properties of MAGeI 3 perovskite solar cells. *Energy Technol.* **11**, (2023).
93. Pindolia, G. & Shinde, S. M. Unleaded all-inorganic KSnI3 perovskite solar cell: a computational study. *Optik (Stuttg).* **295**, 171470 (2023).
94. Pindolia, G. & Shinde, S. M. Potassium tin mixed iodide-bromide KSn(I1-xBrx)3 [x = 0.25,0.5,0.75,1] perovskites for solar cell absorbers: a computational study. *Mater. Sci. Eng. B.* **297**, 116795 (2023).

95. Hossain, M. K. et al. Harnessing the potential of $CsPbBr_3$-based perovskite solar cells using efficient charge transport materials and global optimization. *RSC Adv.* **13**, 21044–21062 (2023).
96. Qi, B. & Wang, J. Fill factor in organic solar cells. *Phys. Chem. Chem. Phys.* **15**, 8972–8982 (2013).
97. Pindolia, G. & Shinde, S. M. Effect of organic charge transport layers on unleaded KSnI3 based perovskite solar cell. *Results Opt.* **12**, 100469 (2023).
98. Pindolia, G., Shinde, S. M. & Jha, P. K. Void of lead and non-carcinogenic germanium based RbGeI3 PSC using organic charge transport layers: towards a clean and green future. *J. Mater. Sci. Mater. Electron.* **34**, 804 (2023).
99. Pindolia, G., Shinde, S. M. & Jha, P. K. Non-leaded, KSnI3 based perovskite solar cell: a DFT study along with SCAPS simulation. *Mater. Chem. Phys.* **297**, 127426 (2023).
100. Bag, A., Radhakrishnan, R., Nekovei, R. & Jeyakumar, R. Effect of absorber layer, hole transport layer thicknesses, and its doping density on the performance of perovskite solar cells by device simulation. *Sol Energy*. **196**, 177–182 (2020).
101. Ahamad, M. & Hossain, A. K. M. A. Design and optimization of non-toxic and highly efficient tin-based organic perovskite solar cells by device simulation. *Heliyon* **9**, (2023).
102. Karmaker, H., Siddique, A. & Das, B. K. Numerical investigation of lead free Cs2TiBr6 based perovskite solar cell with optimal selection of electron and hole transport layer through SCAPS-1D simulation. *Results Opt.* **13**, 100571 (2023).
103. Nowsherwan, G. A. et al. Numerical optimization and performance evaluation of ZnPC:PC70BM based dye-sensitized solar cell. *Sci. Rep.* **13**, 1–16 (2023).
104. Shah, D. K. et al. A simulation approach for investigating the performances of cadmium telluride solar cells using doping concentrations, carrier lifetimes, thickness of layers, and band gaps. *Sol Energy*. **216**, 259–265 (2021).
105. Jaiswal, R. et al. Numerical study of eco-friendly Sn-based Perovskite solar cell with 25.48% efficiency using SCAPS-1D. *J. Mater. Sci. Mater. Electron.* **34**, (2023).
106. Jamal, M. S. et al. Effect of defect density and energy level mismatch on the performance of perovskite solar cells by numerical simulation. *Optik (Stuttg).* **182**, 1204–1210 (2019).
107. Darvishzadeh, P., Redzwan, G., Ahmadi, R. & Gorji, N. E. Modeling the degradation/recovery of short-circuit current density in perovskite and thin film photovoltaics. *Org. Electron.* **43**, 247–252 (2017).
108. Ahmed, A., Riaz, K., Mehmood, H., Tauqeer, T. & Ahmad, Z. Performance optimization of CH3NH3Pb(I1-xBrx)3 based perovskite solar cells by comparing different ETL materials through conduction band offset engineering. *Opt. Mater. (Amst)* **105**, (2020).
109. An, Y. et al. Perovskite solar cells: optoelectronic simulation and optimization (solar RRL 11/2018). *Sol RRL* **2**, (2018).
110. Hossain, M. K. et al. Design and simulation of Cs_2BiAgI_6 double perovskite solar cells with different electron transport layers for efficiency enhancement. *Energy Fuels*. **37**, 3957–3979 (2023).
111. Pindolia, G., Pandya, J., Shinde, S. & Jha, P. K. Fluorinated copper phthalocyanine as an electron transport material in perovskite solar cell. *Int. J. Energy Res.* **46**, 15127–15142 (2022).
112. Anwar, F., Mahbub, R., Satter, S. S. S. & Ullah, S. M. M. Effect of different HTM layers and electrical parameters on ZnO nanorod-based lead-free perovskite solar cell for high-efficiency performance. *Int. J. Photoenergy* 1–9 (2017). (2017).
113. Hasanzadeh Azar, M. et al. SCAPS empowered machine learning modelling of perovskite solar cells: predictive design of active layer and hole transport materials. *Photonics* **10**, 271 (2023).
114. Karthick, S., Velumani, S. & Bouclé, J. Experimental and SCAPS simulated formamidinium perovskite solar cells: a comparison of device performance. *Sol Energy*. **205**, 349–357 (2020).
115. Glowienka, D. & Galagan, Y. Light intensity analysis of photovoltaic parameters for perovskite solar cells. *Adv. Mater.* **34**, (2022).
116. Mesquita, I., Andrade, L. & Mendes, A. Temperature impact on perovskite solar cells under operation. *ChemSusChem* **12**, 2186–2194 (2019).
117. Meng, Q. et al. Effect of temperature on the performance of perovskite solar cells. *J. Mater. Sci. Mater. Electron.* **32**, 12784–12792 (2021).
118. Pindolia, G., Shinde, S. M. & Jha, P. K. Optimization of an inorganic lead free RbGeI3 based perovskite solar cell by SCAPS-1D simulation. *Sol Energy*. **236**, 802–821 (2022).
119. Pindolia, G., Shinde, S. & Jha, P. K. P3CPenT as an organic hole transport layer for perovskite solar cells. *Int. J. Quantum Chem.* **123**, e27149 (2023).

Acknowledgements

The authors gratefully acknowledge Dr. M. Burgelman of the University of Gent, Belgium, for providing the SCAPS-1D program (version 3.3.10) used in this research. The software is available at https://scaps.elis.ugent.be/. The authors would like to express their gratitude to him. This work was funded by the Researchers Supporting Project Number (RSP2024R265) King Saud University, Riyadh, Saudi Arabia.

Author contributions

M.K. Hossain: Conceptualization, Methodology, Software, Validation, Formal analysis, Investigation, Data curation, Writing – original draft, Writing – review & editing, Supervision, Project administration; M.A. Islam: Formal analysis, Writing – original draft; M.S. Uddin: Software, Validation, Formal analysis, Investigation, Data curation; P. Paramasivam: Validation, Investigation, Formal analysis, Writing – review & editing; J.A. Hamid, R.A. Alshgari, V. K. Mishra, and R. Haldar: Validation, Formal analysis, Writing – review & editing.

Declarations

Competing interests

The authors declare no competing interests.

Additional information

Correspondence and requests for materials should be addressed to M.K.H., P.P., V.K.M. or R.H.

Reprints and permissions information is available at www.nature.com/reprints.

Publisher's note Springer Nature remains neutral with regard to jurisdictional claims in published maps and institutional affiliations.